Intelligent Wind Estimation for Chemical Source Localization

Jared Cooper
Senior Research Scientist
Barron Associates, Inc.
Charlottesville, VA, USA

Jeremy Hopwood
Phd Candidate
Aerospace and Ocean
Engineering, Virginia Tech
Blacksburg, VA, USA

Craig Woolsey
Professor
Aerospace and Ocean
Engineering, Virginia Tech
Blacksburg, VA, USA

Stephan De Wekker
Professor
Environmental Sciences,
University of Virginia
Charlottesville, VA, USA

Michael DeVore
Principal Scientist
Barron Associates, Inc.
Charlottesville, VA, USA

ABSTRACT

This paper presents a methodology to sense ambient wind conditions to assist in localizing the source of a released agent using small unmanned aerial systems (sUAS). The release of chemical, biological, radiological, or nuclear (CBRN) agents is a long-standing threat to populated areas and to ecosystems, in general. Such agents could be released intentionally by an adversary, accidentally, or by means of natural disaster. The technology and methods to detect, localize, and model release and dispersion of CBRN agents have been enhanced by integrating cross-disciplinary solutions using advances from sensor design, intelligent signal processing, control systems, vehicle design, chemical modeling, and atmospheric modeling. The miniaturization of sensors and sUAS has enabled the application of sUAS with a chemical sensor payload to detect and localize the source of CBRN agents. In many instances, this chemotaxis operation can be performed faster and more accurately with the addition of atmospheric information, such as ambient wind condition. The paper provides an overview of chemical source localization and current challenges which motivated this work, including operation in complex settings and turbulence. Analysis of these challenges from an atmospheric science perspective is summarized along with strategies to obtain accurate and useful wind estimates that assist in localizing the source quickly and efficiently. A description of the wind estimation approach, based on Bayesian estimation, is provided along with results from simulation studies utilizing realistic vehicle dynamics, wind, turbulence, and chemical plume models.

INTRODUCTION

This paper presents a methodology to estimate ambient wind conditions to use as a command control signal for autonomous small unmanned air systems (sUAS) to locate the source of a released agent. The wind estimator can be combined with different source localization approaches to localize the source quickly and with certainty. The release of chemical, biological, radiological, or nuclear (CBRN) agents is a long-standing threat to populated areas as well as other plant and animal populations, and ecosystems, in general. Such agents could be released intentionally by an adversary, accidentally, or by means of natural disaster. The technology and methods to detect, localize, and model the release and dispersion of CBRN agents have been enhanced by integrating cross-disciplinary solutions with advances from sensor design, intelligent signal processing, control systems, vehicle design, chemical modeling, and atmospheric modeling. The miniaturization of sensors and sUAS has enabled the application of sUAS with a chemical sensor payload to detect and localize the source of CBRN agents. In many instances, this chemotaxis operation can be performed faster and more accurately with the addition of atmospheric information, such as ambient wind condition.

The literature is rich in the areas of wind estimation and chemical source localization using a variety of means, including static and mobile sensors. This paper presents research that uses the sUAS itself as a pseudo wind sensor instrumented with a chemical detector. *Indirect wind estimation* is used where the vehicle itself is treated as the wind sensor (Refs. 1–3). Estimates of the ambient wind are obtained using outputs of sensors common to most autopilots and a dynamic model of the sUAS. This approach differs from *direct wind estimation* where a sUAS is instrumented with

Presented at the Vertical Flight Society's 79th Annual Forum & Technology Display, West Palm Beach, FL, USA, May 16–18, 2023.

some type of anemometer to measure the ambient winds directly (Refs. 4, 5).

One of the key benefits of the wind estimator developed in this paper is the ability to accurately estimate winds during maneuvering and non-hovering flight. Due to a requirement to limit the time and frequency at which the vehicle hovers to sample wind and concentration data, a model that estimates winds at potentially large advance ratios and general flight maneuvers is required. The simplistic *hover models* often seen in the literature, where the rotor thrust and torque are modeled as a constant multiplied by the square of the rotor rotational speed, do not meet program requirements, and introduce uncertainty and error in the estimation algorithm. One purpose of this paper is to present a model suitable for general flight conditions based on first-principles and then refined with system identification techniques. The development focuses on the forces and moments generated by the rotors, following blade-element theory, with appropriate simplifications for a multi-rotor without swashplate controls.

The remainder of this paper provides a brief overview of chemical source localization and current challenges which motivated this work, including operation in complex settings and turbulence. Analysis of these challenges from an atmospheric science perspective provides strategies to obtain accurate and useful wind estimates that assist in localizing the source quickly and efficiently. A description of the wind estimation approach, based on Bayesian estimation, is provided along with results from simulation studies utilizing realistic vehicle dynamics, wind, turbulence, and chemical plume models.

SOURCE LOCALIZATION

A number of approaches are reported in the literature for gas or pollutant source localization, also called source seeking (SS). These approaches can be generally classified as exploration approaches inspired by biological agents, e.g., chemotaxis and anemotaxis; optimization approaches; probabilistic methods (Bayesian inference); and hybrid approaches (Ref. 6). Anemotaxis refers to the movement of an organism in response to the motion of a surrounding fluid, e.g., an organism moving in a sensed upwind direction in search of a food source. Chemotaxis is the movement of an organism in response to a chemical stimulus, such as the change in a gradient, where an organism would move towards the highest concentration of a sensed agent. A few of the more popular biologically inspired approaches include the biased random walk of the E. coli bacterium; surge-casting mimicking the male silkworm moth, which has similarities to the tracking behavior of the male Tobacco Hornworm moth (Ref. 7), and a zig-zag approach observed in the dung beetle (Refs. 8, 9). Examples of the surge-casting and zig-zag motion strategies are depicted in Figure 1a and 1b, respectively. Other approaches use gradient descent, particle filters, particle swarm optimization, and Bayesian inference networks (Ref. 10).

In addition to chemical gradient and flow information, statistical descriptions of the turbulent flow have been suggested

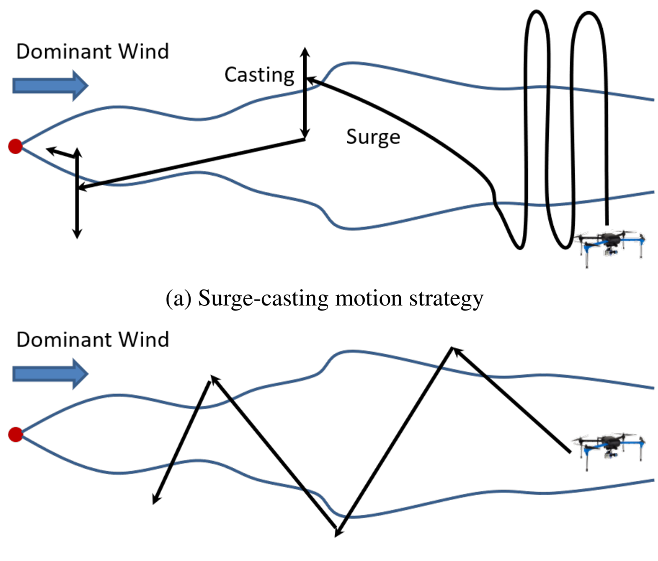

(a) Surge-casting motion strategy

(b) Zig-zag motion strategy

Figure 1. Biologically inspired motion strategies

to be used by natural organisms. In (Ref. 11), the authors suggest the *Panilus argus* (spiny lobster) uses active bursting olfactory receptor neurons (bORN) to encode the time between encounters which supplements fluid flow direction and magnitude detected by other mechanosensory cells. This work suggests using an *intermittency* measure to guide the search direction to lead the agent to track the edge of the plume, as opposed to the plume centerline seen in concentration (chemotactic) approaches, and yield a reduced search time. In (Ref. 12), the authors note that walking *Drosophila melanogaster* direct motion upwind based on the frequency of encounter with an odor and the intermittency of the odor signal. This research suggests that using both intermittency and mean gradient signals may be advantageous in certain environments, but a weighting is desired in general application. In practice, biological systems may be able to react more quickly than cyber-physical systems owing to superior sensing and processing systems. As such, sensor characteristics like the response time and noise characteristics should be considered in developing search strategies informed by biological systems. Effects of the UAS platform should also be considered, e.g., the rotor wake generated by multi-rotor UAS can distort the sensed ambient wind (Ref. 4) (if using a direct wind sensor) and chemical concentration readings.

Past research efforts have evaluated source localization approaches in simplified conditions with steady constant airflow, neglected turbulence, or did not include buildings or other obstacles that naturally create turbulent conditions. Even in open environments, the level of atmospheric instability will affect turbulence intensity and characteristics leading to uneven concentration levels and complex plume structures. Results have varied when evaluating different chemotaxis and anemotaxis approaches in realistic test environments. In (Ref. 9), the authors note that "...plume tracking is possible under certain circumstances in the real-world, it is difficult to locate gas sources in scenarios with changing wind conditions and high turbulence." Some reports indicate chemotaxis-only approaches were brittle in turbulent conditions; however, performance improvements were observed when combining chemotaxis and anemotaxis methods (Ref. 6). The wind estimation approach presented in this paper is agnostic to the source localization method and could enhance the performance of the aforementioned source localization methods. Many profitable techniques can be learned from natural organisms, including operation in turbulent and urban environments. The following section augments these biologically-inspired approaches with an understanding of the atmospheric conditions and suggests strategies to sample wind information in regions with complex flow and dispersion patterns.

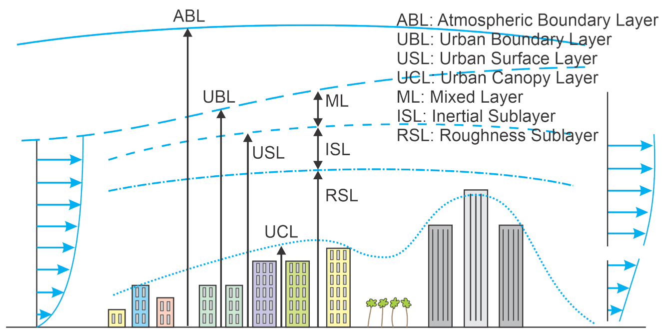

Figure 2. Description of urban boundary layers (adapted from (Ref. 15))

ATMOSPHERIC CONSIDERATIONS

The successful documentation and modeling of complex terrain and urban flows is of utmost importance for various disciplines including architects and city planners, chemical and biological transport analysis, military operations, UAS operations, e.g., package delivery, and personal air vehicles such as the urban air mobility (UAM) concepts. Progress towards understanding flows and turbulence in the urban atmosphere and its effect on, for example, dispersion conditions has been slow in large part because of experimental difficulties. A major reason is the large degree of spatial and temporal heterogeneity of these flows that makes data collection a challenge. The flow in the roughness sublayer (RSL) is strongly influenced by the wakes of roughness elements such as individual buildings, as shown in Figures 2 - 4. The resulting spatiotemporal variability is challenging to sample in three dimensions at sufficient resolution. Consequently, atmospheric transport and dispersion models have poor performance at the building scale because of the assumptions underlying these models, e.g., horizontal homogeneity. For this reason, computational fluid dynamics (CFD) models have been developed in recent years with some comparisons to empirical data (Ref. 13).

A classification of various zones in the atmosphere over urban areas consists of the urban boundary layer (UBL), urban canopy layer (UCL), and roughness sublayer (RSL) (Ref. 14). As depicted in Figure 2, the UCL extends to the average building height while the RSL extends to multiple ($\approx$ 2–5) times the average building height. Of most interest for this paper are processes up to the height of the RSL with a focus on conditions close to the urban surface and inside street canyons.

To gain appreciation of the flow variation around these building structures, Figure 3 illustrates the 3D winds for an upwind direction of 355^o. Arrows indicate wind speed and direction where a non-uniform spacing technique was applied to assist in visualizing flows that vary from the upwind condition. Specifically, the arrow length indicates a proportional change in wind magnitude from the upwind location, where the arrow size at the highest elevation is a reference for the upwind magnitude, and arrow color indicates angular deviation. Stagnation points are visible as the wind impinges the face of the buildings, as are creation of wake vortices on the leeside of the buildings, indicated by large reversals of wind direction. Urban canyon effects are also visible, creating wind shears and channeled flows. Figure 4 depicts a streamline plot at four meters elevation where the creation of vortices on the leeside of the buildings is more visible.

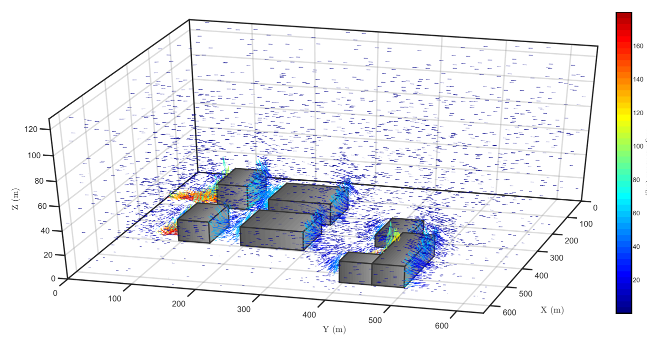

Figure 3. Example wind profile

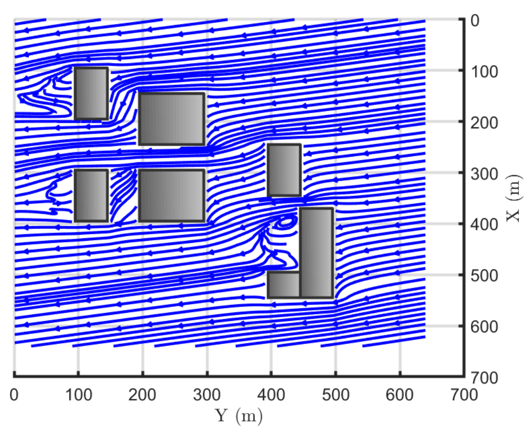

Figure 4. Wind streamlines at 4m AGL

The wind flow and turbulence have a direct impact on the dispersion of the released agent, but tracer and agent dispersion

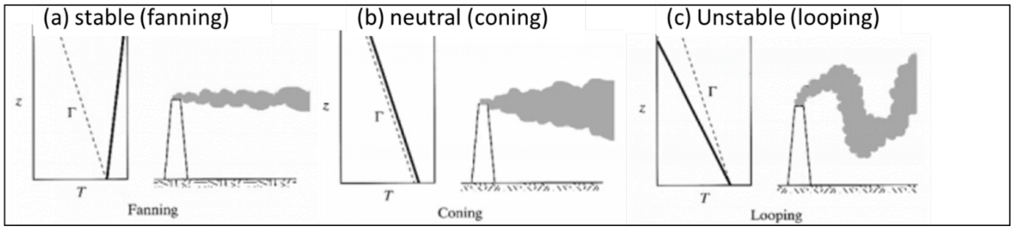

Figure 5. Plume shape from a continuously emitting source in a) stable, b) neutral, and c) unstable atmospheric conditions (adapted from (Ref. 16))

is also governed by atmospheric stability. Atmospheric stability refers to the ability of the atmosphere to allow vertical motions and is determined using vertical gradients in temperature and in moisture content. Many simplified models do not consider stability effects of atmospheric flows and dispersion since they assume a so-called neutral atmosphere. A neutral atmosphere means that the atmospheric temperature decreases by 1^oC per 100 m increase in height. For an unstable (stable) atmosphere, this decrease in temperature with height is more (less) than 1^oC per 100 m. If the temperature increases with height, this is also called a temperature inversion. Atmospheric vertical temperature profiles typically have discontinuities, and the changes in humidity associated with the temperature discontinuities are usually quite pronounced. During daytime, the atmosphere is typically unstable and during nighttime, typically stable.

It is well known that atmospheric stability affects atmospheric dispersion and flows, including the flow pattern around buildings. If a source localization algorithm wants to take advantage of this knowledge, it is important that temperature measurements are made on the UAS along with wind and tracer concentration measurements. To illustrate some of the complexities associated with sampling useful mean and turbulence information from sUAS for the purpose of source localization, consider the shape of a tracer plume in a stable, neutral, and unstable atmosphere as shown in Figure 5. For the same mean wind speed and direction, the transport of the plume will be similar for these conditions. However, the turbulence determines whether a plume will stay very confined (fanning/coning for the case of a stable/neutral atmosphere and weak/moderate turbulent diffusion) or whether there is large vertical transport of the plume (looping for the case of an unstable atmosphere and strong turbulent diffusion). In the left-side panel of each subfigure z refers to elevation above ground, T atmospheric temperature, and Γ the dry adiabatic lapse rate. The dashed line indicates the dry adiabatic lapse rate and serves as a baseline for comparison with the environmental, or current, lapse rate shown with the solid line.

For a UAS that takes measurements at moderate distances downwind of a release point, the likelihood of detecting the tracer is much more likely near the height of the release point in the stable case than in the unstable case. On the other hand, the likelihood of detecting the tracer is much more likely at higher elevations in the unstable case than in the stable case. If the source detection algorithm includes a vertical profile to detect the source, the height at which the tracers are first observed along with the vertical temperature gradient and observed winds, can provide an initial guess of the source distance using a simple Gaussian plume model if on-board computational resources are limited.

MULTI-ROTOR AERODYNAMICS

This section develops a general model for multi-rotor vehicles that can be used in model-based estimation approaches, such as the Bayesian estimator used in this paper. Due to a program requirement to limit the time and frequency at which the vehicle hovers to sample wind and concentration data, a process model that captures dynamic flight at potentially large advance ratios and general flight maneuvers is required. The simplistic *hover* models often seen in the literature, where the rotor thrust and torque are modeled as a constant multiplied by the square of the rotor rotational speed, do not meet program requirements and introduce uncertainty and error in the estimation algorithm. The rotor H-force, sometimes called the rotor drag, should also be included as can a pitching moment generated by the rotor. Due to symmetry of some multi-rotor vehicles, some papers remove the rolling moments produced by the rotors; however, this term is retained for the formulation presented in this paper. A generalization is also made that allows the rotor hub frame to be rotated relative to the body-frame. Blade flapping is included in the derivation to illustrate that the flapping motion creates an effective drag force, in addition to the H-force, that is linearly dependent on airspeed. Past research (Ref. 1) has shown that at low to moderate speeds the drag from the H-force and flapping terms is the dominant drag force. The H-force and flapping drag effects are combined later in the paper when system identification techniques are used to estimate parameters of a postulated model structure. The parasitic drag from the fuselage, dependent on the square of airspeed, becomes the dominant drag force at higher speeds.

A summary of quadrotor aerodynamics is provided following the generation of blade forces and moments developed using blade element theory (BET). The material largely follows that of Johnson (Ref. 17) but also borrows from Prouty (Ref. 18) and Leishman (Ref. 19). A general vehicle model structure is derived from this analysis of the rotor forces and moments. The parameters of the model structure are then identified using system identification with surrogate flight data generated from a high-fidelity multi-rotor simulation (Ref. 20). The system identification approach uses statistically-sound algorithms to guide model creation in a semi-automated, or completely automated, process (Refs. 21, 22). The overall approach is founded on maximum likelihood estimation theory and is applicable to different vehicle types, requiring a fraction of the data needed for deep learning approaches.

Multi-rotor Dynamics

In many respects a quadrotor is a simplified version of traditional rotary-wing vehicles such as helicopters and tiltrotors. The simplification arises from multiple sources such as the symmetry of the vehicle design, eliminating cross-coupling terms in the moment of inertia tensor, and lack of a swashplate on the rotor system, replaced with direct speed control of the rotors with fixed-pitch blades. The dynamic model implemented for this program uses a rigid-body formulation and assumes rigid blade flapping but that blade elastic deformation and lead-lag motion are negligible. The derivation generally follows that found in helicopter aerodynamic theory with simplifying assumptions noted. The resulting equations guide the selection of a process model suitable for general flight to be used in the wind estimation algorithm.

Consider a multi-rotor aircraft, modeled as a rigid body of mass m. Let unit vectors $\{\boldsymbol{x}_I, \boldsymbol{y}_I, \boldsymbol{z}_I\}$ define an earth-fixed, local geodetic, inertial North-East-Down (NED) orthonormal reference frame, $\mathscr{F}_{\mathrm{I}}$, as shown in Figure 6a. Let the unit vectors $\{\boldsymbol{x}_b, \boldsymbol{y}_b, \boldsymbol{z}_b\}$ define the orthonormal body-fixed frame, $\mathscr{F}_{\mathrm{B}}$, centered at the aircraft center of mass where the $\boldsymbol{x}_b$-$\boldsymbol{y}_b$ plane defines the aircraft's horizontal plane and $\boldsymbol{z}_b$ points out the bottom. The body frame follows common aerospace notation with the positive x-axis pointing out the nose and the positive y-axis out the right wing.

Define a rotor hub frame with the unit vectors $(\boldsymbol{x}_h, \boldsymbol{y}_h, \boldsymbol{z}_h)$. The rotor hub frame has the $\boldsymbol{z}_h$ axis aligned with the rotor shaft and pointing down, the $\boldsymbol{x}_h$ axis points out the nose, as $\boldsymbol{x}_b$, but may be rotated by some angle θ_h about $\boldsymbol{y}_h$ to align $\boldsymbol{z}_b$ with the rotor shaft, and $\boldsymbol{y}_h$ completes a right-hand frame. In general, the rotor hub frame may be rotated relative to the body-frame by angles $(\phi_h, \theta_h, \psi_h)$. If these angles are all zero, then the rotor hub frame is parallel to the body-frame.

The position of the body frame with respect to the inertial frame is given by the vector $\boldsymbol{r} = [x\ y\ z]^\top$. The attitude of the aircraft is given by the rotation matrix, $\boldsymbol{R}^{\mathrm{I}}_{\mathrm{B}}$, that maps free vectors in $\mathscr{F}_{\mathrm{B}}$ to $\mathscr{F}_{\mathrm{I}}$. Consider the Euler angle parameterization:

$$\boldsymbol{R}^{\mathrm{I}}_{\mathrm{B}} = e^{[e_3\times]\psi} e^{[e_2\times]\theta} e^{[e_1\times]\phi}$$

where ϕ, θ, and ψ are the roll, pitch, and yaw angles of the aircraft, respectively. Here, $\boldsymbol{e}_1 = [1\ 0\ 0]^\top$, etc., and $[(\cdot)\times]$ is the skew-symmetric cross product equivalent matrix satisfying $[\boldsymbol{a}\times]\boldsymbol{b} = \boldsymbol{a}\times\boldsymbol{b}$. Let $\boldsymbol{V}_b = [u\ v\ w]^\top$ and $\boldsymbol{\omega} = [p\ q\ r]^\top$ be

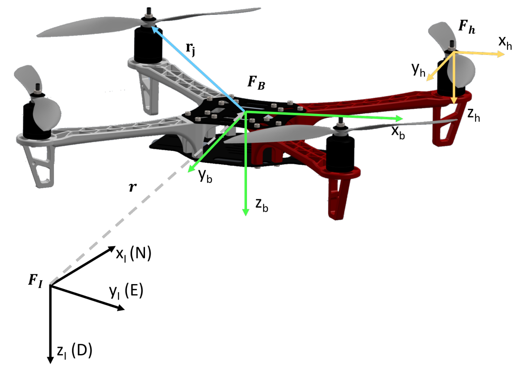

(a) Primary reference frames

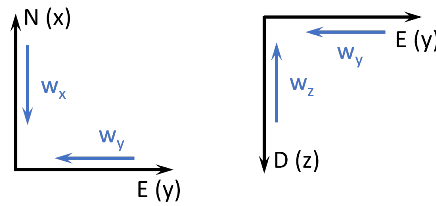

(b) Inertial and steady-state wind frames

Figure 6. Primary reference frames and wind direction

the translational and rotational velocity of the aircraft with respect to $\mathscr{F}_{\mathrm{I}}$ expressed in $\mathscr{F}_{\mathrm{B}}$, respectively. With this choice of Euler angles, the kinematic equations of motion are:

$$\dot{\boldsymbol{r}} = \boldsymbol{R}^{\mathrm{I}}_{\mathrm{B}} \boldsymbol{V}_b \tag{1a}$$

$$\dot{\boldsymbol{R}}^{\mathrm{I}}_{\mathrm{B}} = \boldsymbol{R}^{\mathrm{I}}_{\mathrm{B}} [\boldsymbol{\omega}\times] \tag{1b}$$

With $\boldsymbol{\Theta} := [\phi\ \theta\ \psi]^\top$, Eq. (1b) becomes

$$\dot{\boldsymbol{\Theta}} = \boldsymbol{L}_{\mathrm{IB}}\boldsymbol{\omega} = \begin{bmatrix} 1 & \sin\phi\tan\theta & \cos\phi\tan\theta \\ 0 & \cos\phi & -\sin\phi \\ 0 & \sin\phi\sec\theta & \cos\phi\sec\theta \end{bmatrix} \begin{bmatrix} p \\ q \\ r \end{bmatrix} \tag{2}$$

The forces and moments on the aircraft expressed in $\mathscr{F}_{\mathrm{B}}$ are a summation of effects from the aerodynamics, rotors, and gravity: $\boldsymbol{F} = [X\ Y\ Z]^\top$ and $\boldsymbol{M} = [\mathscr{L}\ \mathscr{M}\ \mathscr{N}]^\top$.

$$\mathbf{F} = m\left(\dot{\mathbf{V}}_b + \boldsymbol{\omega}_b \times \mathbf{V}_b\right) = \mathbf{F}_A + \mathbf{F}_R + \mathbf{F}_G \tag{3}$$

$$\mathbf{M} = I_b\dot{\boldsymbol{\omega}}_b + \boldsymbol{\omega}_b \times I_b\boldsymbol{\omega}_b = \mathbf{M}_A + \mathbf{M}_R \tag{4}$$

where I_b is the moment of inertia matrix about the center of mass in $\mathscr{F}_{\mathrm{B}}$, the subscript A indicates the forces and moments generated by the airframe or all non-rotating elements, the subscript R indicates the forces and moments generated by the rotors, and G indicates inertial forces. Due to symmetry the cross-coupling inertia terms are assumed negligible. The components of the external force vector $\mathbf{F}$ and moment vector $\mathbf{M}$ are the summed contributions of each subsystem in the given direction.

Velocity in the inertial frame $\mathscr{F}_{\mathrm{I}}$, is expressed by the vector $\mathbf{V}^I_b = \boldsymbol{R}^{\mathrm{I}}_{\mathrm{B}}\mathbf{V}_b$. The rotation matrix is orthonormal, so the inverse can be found by taking the transpose which provides a rotation from the inertial to body frame $\boldsymbol{R}^{\mathrm{B}}_{\mathrm{I}}$. Winds and turbulence are generated in the inertial frame with a positive direction opposite to that of the inertial frame, so the airspeed vector in the inertial frame is $\mathbf{V}_a^I = \mathbf{V}_b^I + \mathbf{V}_w^I$, where $\mathbf{V}_w^I = [w_x, w_y, w_z]^T$ is the wind velocity expressed in the inertial frame. In this manner the winds are added to the inertial velocity of the vehicle to produce an airspeed relative to the airmass. Figure 6b illustrates the inertial and wind frames.

Rotor Velocities

This section describes the motion and velocities used by a rotor system. Figure 7a illustrates the motion of the rotor with respect to a reference frame and free stream velocity $\mathbf{V}_{a,h}$ which is at an incidence angle i relative to the rotor reference frame. The incidence angle i is positive in forward flight conditions with a forward tilt of the rotor disc. The development in this section uses the incidence angle to derive rotor velocities which offers a natural choice for rotor analysis. However, for modeling a vehicle with flight data, body-velocities can be preferable and so in subsequent sections, the rotor forces and moments are expressed with velocities in the body axis. As shown here, the reference frame depicts a forward flight condition and the reference frame is the hub frame rotated by 180^o about the $\boldsymbol{y}_h$ axis. For general flight conditions the reference frame is rotated by an angle ψ_{hw} about the $\boldsymbol{z}$ axis so the $\boldsymbol{y}$ component of $\mathbf{V}_{a,h}$ is zero, as shown in Figure 7a. The out-of-plane blade motion is described by the flapping angle $\beta(\psi)$ and is a function of the azimuth angle ψ. The blade pitch is $\theta(r)$ described as the angle of the blade relative to the reference plane and varies with radial station, r.

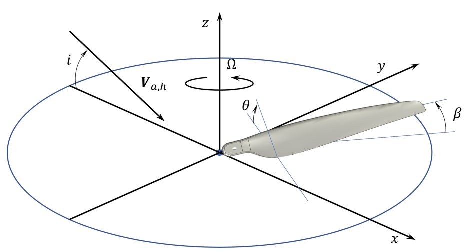

(a) Rotor motion and velocity relative to a reference frame

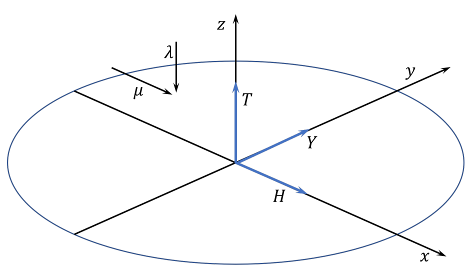

(b) Rotor forces and dimensionless velocities

Figure 7. Rotor motion, velocities, and forces relative to a defined reference frame (adopted from (Ref. 17))

The rotor forces defined in the reference frame are shown in Figure 7b and include the thrust T, the H-force H which is a drag force acting along the reference plane, and a sideforce Y. The free stream velocity at the rotor hub is a combination of the velocity at the vehicle CG, rotational rates, and winds, expressed in the body-frame as:

$$\mathbf{V}_{a,h}^b = \left(\mathbf{V}_b + R_I^b \mathbf{V}_w^I\right) + \omega \times \mathbf{r}_j \tag{5}$$

where ω is the vehicle rotational rate and $\mathbf{r}_j$ is a vector from the vehicle CG to the j^{th} rotor, see Figure 6a. Non-dimensional velocities μ, the advance ratio, and λ, the normalized inflow ratio, are also introduced in this figure. These velocities are the non-dimensional components of $\mathbf{V}_{a,h}$ parallel and perpendicular to the reference frame, respectively, and are defined as:

$$\begin{aligned}\mu &= \frac{\mathbf{V}_{a,h}\cos i}{\Omega R} \\ \lambda &= \frac{\mathbf{V}_{a,h}\sin i + \nu}{\Omega R} = \mu \tan i + \lambda_i + \lambda_c \cos i\end{aligned} \tag{6}$$

where ν is the inflow velocity, λ_i is the induced inflow ratio, and $\lambda_c = V_c/(\Omega R)$ is the climb ratio and V_c is the climb rate. This equation for induced inflow applies to horizontal and vertical flight and can be found with momentum theory (Ref. 19). First define the dimensional induced inflow:

$$\nu = \frac{\nu_h^2}{\sqrt{\left(\mathbf{V}_{a,h}\cos i\right)^2 + \left(\mathbf{V}_{a,h}\sin i + \nu\right)^2}} \tag{7}$$

where $\nu_h^2 = T/2\rho A$ is the inflow at hover. Define $V_x = \mathbf{V}_{a,h}\cos i$ and $V_z = \mathbf{V}_{a,h}\sin i$. For multi-rotors with N_{rot} rotors, equal thrust sharing is assumed at hover, such that:

$$\nu_h^2 = \frac{mg/N_{rot}}{T/2\rho A} \tag{8}$$

The inflow ratio normal to the rotor disc is:

$$\mu_z = \frac{V_z}{\Omega R} = \frac{\mathbf{V}_{a,h}\sin i}{\Omega R} = \mu \tan i \tag{9}$$

and note the induced inflow ratio at hover $\lambda_h = \sqrt{C_T/2}$. The induced inflow ratio λ_i can then be written as:

$$\lambda_i = \frac{\nu}{\Omega R} = \frac{\lambda_h^2}{2\sqrt{\mu^2+\lambda^2}} = \frac{C_T}{2\sqrt{\mu^2+\lambda^2}} \tag{10}$$

From this the general form of the inflow equation is derived, which can usually be solved efficiently with a numerical routine:

$$\lambda = \mu \tan i + \frac{C_T}{2\sqrt{\mu^2+\lambda^2}} + \lambda_c \cos i \tag{11}$$

If the rotor is in edgewise flight, $i = 0$, there is an exact solution for induced velocity (Ref. 18):

$$\nu^2 = -V^2/2 + \sqrt{(V^2/2)^2 + \nu_h^4} \tag{12}$$

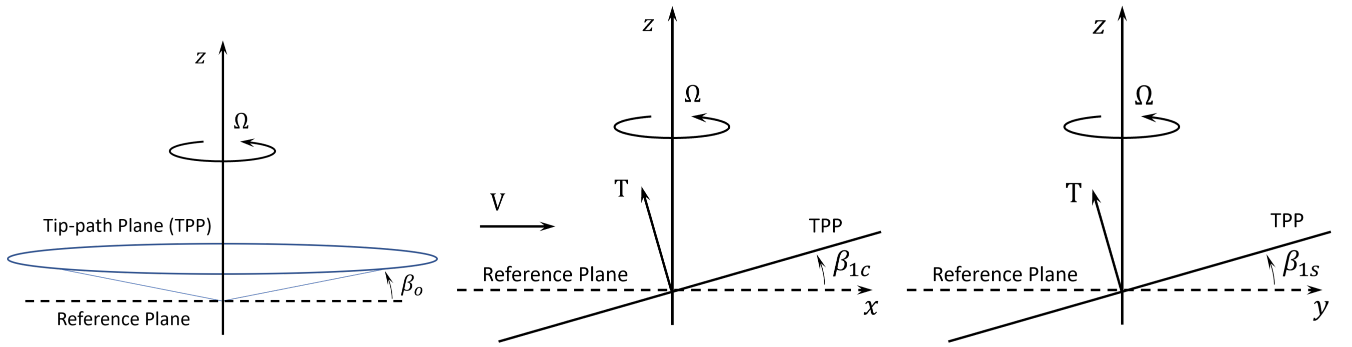

(a) Rotor coning (b) Longitudinal flap angle (view from left) (c) Lateral flap angle (view from aft)

Figure 8. First-order harmonic blade flapping motion (adopted from (Ref. 17))

Blade Geometry & Flapping

The blade pitch and chord varies with radial station. The blade pitch can be approximated with a linear twist distribution as $\theta(r) = \theta_o + \theta_{tw} r$ where θ_o is the pitch at the blade root and θ_{tw} is the slope of the pitch variation along radial station r. A linear twist model is used since the inboard sections of the blade generate small forces due to low dynamic pressure. A linear variation with chord could also be used but an average chord value is used in this work.

The blade coning and flapping represents the out-of-plane motion the blade experiences as it rotates, caused by an asymmetric aerodynamic environment in forward flight. The motion is periodic with a fundamental frequency equal to that of the rotor speed, Ω, and can be represented with a Fourier series, where only the first harmonic terms are retained:

$$\beta(\psi) = \beta_o + \beta_{1c} \cos\psi + \beta_{1s} \sin\psi \tag{13}$$

Each term can be explained when viewed in the non-rotating frame as shown in Figure (8). The mean-value of the flap angle is given by β_o and is known as the coning angle. As seen in Figure 8a β_o causes the blades to deflect by the same angle independent of azimuth position. The tips of the blades trace a plane through space parallel to the reference (xy) plane and is called the tip-path plane (TPP). *Pure coning*, or the absence of longitudinal and lateral flap, occurs at hover and in axial flight under normal operating conditions. Longitudinal tilt of the TPP is described by the angle β_{1c} and the lateral tilt by β_{1s}. Thus, the orientation of the TPP relative to the non-rotating frame is provided by the angles β_{1c} and β_{1s}.

The thrust T is perpendicular to the TPP and rotated by the first-harmonic blade flap angles relative to the non-rotating frame. The aft tilt of the thrust vector relative to the free stream velocity creates a drag term and the lateral tilt creates a sideforce term. The blade-flapping motion creates an effective drag term that, combined with the rotor H-force, is the dominant drag source for low to moderate advance ratio flight. In the following section that discusses the full vehicle model structure, the blade flap effects are lumped together with the H-force with a term that is linearly dependent on airspeed.

Rotor Aerodynamics: Blade Element Theory

This section provides an overview of rotor aerodynamics based on blade-element theory and is suitable for the vehicle at hover, forward flight, and axial flight; however, the presentation will focus on the vehicle in forward flight. The following simplifying assumptions are made:

1. Rigid blade flapping is the only blade motion, i.e., elastic blade deformation and lead-lag motion is assumed negligible
2. Tip loss, root cutout, and the effects of the reverse flow region are ignored
3. Rotor speed control is active and is there is no collective or cyclic pitch inputs
4. Sufficiently accurate modeling can be achieved with an averaged uniform inflow model
5. The aerodynamics at a blade section, or element, can be captured with two-dimensional airfoil theory such that the influence of the rotor wake is simplified to an induced velocity at the blade element.
6. Compressibility and stall effects are assumed negligible.

The motion and forces generated by the entire rotor relative to a reference frame are first described, followed by analysis of the forces at a blade element a distance r from the center of rotation. The blade element forces are integrated along the rotor radius and over one complete revolution to arrive at the forces and moments generated by the rotor.

The velocities and forces acting on the blade element are presented in Figure 9a where a non-rotating reference frame is used to measure the angles. The components of the velocity of the air relative the blade section consist of the tangential u_T and perpendicular u_P components. The angle ϕ is called the inflow angle. The following relationships are found:

$$V = \sqrt{u_T^2 + u_P^2}$$

$$\phi = \tan^{-1}\left(\frac{u_P}{u_T}\right)$$

$$\alpha = \theta - \phi$$

The tangential velocity component can be written in non-dimensional form by recalling the velocity of the rotor hub from Eq. (5) and adding to this the velocity given by the rotor rotation at blade element r. The tangential velocity of a blade element in the non-rotating reference frame is (note expression of the velocity in the body-frame is dropped here):

$$U_T = r\Omega + V_{a,h}\cos(i)\sin(\psi) \underset{\text{normalize}}{\longrightarrow} u_T = r + \mu\sin(\psi) \quad (14)$$

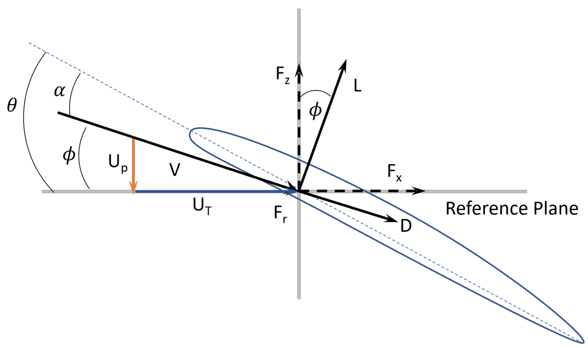

(a) Forces and velocities at a rotor element (looking outboard)

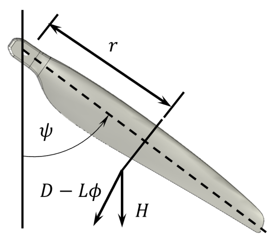

(b) Forces and velocities at a rotor element (top view)

Figure 9. Inspection of forces and velocities for a rotor element

The velocity perpendicular to the reference plane has three terms: 1) the induced velocity plus the component of the free stream velocity normal to the rotor disc, $\Omega R\lambda$, where $\lambda = \mu i + \lambda_i$, 2) the angular velocity of the blade about the flap hinge point, $r\frac{d\beta}{dt}$, and a component of the radial velocity normal to the blade when the blade flaps by the angle β, $\Omega R\beta\mu\cos\psi$. The non-dimensional form of the perpendicular velocity is then:

$$u_P = \lambda + r\dot{\beta} + \beta\mu\cos\psi \quad (15)$$

The elemental forces are also shown in Figure 9a where the lift (L) is normal to the resultant velocity, drag (D) is parallel to the velocity and opposes the blade motion. These forces can be resolved into the axes of the reference frame as F_x, F_z, and a radial force F_r that is positive when pointing outboard.

The lift and drag resolved in the reference frame yields:

$$F_z = L\cos\phi - D\sin\phi \quad (16)$$
$$F_x = L\sin\phi + D\cos\phi \quad (17)$$
$$F_r = -\beta F_z \quad (18)$$

A number of simplifying assumptions are now made including the small angle assumption and neglecting stall and compressibility effects. The following simplified expressions for the forces, written in non-dimensional form, are found where both sides are divided by the lift-curve slope, a, and average chord, c:

$$F_z \cong L \longrightarrow \frac{F_z}{ac} = \frac{1}{2}u_T^2\alpha = \frac{1}{2}\left(u_T^2\theta - u_P u_T\right) \quad (19)$$
$$F_x \cong L\phi + D \longrightarrow \frac{F_x}{ac} = u_T^2\left(\frac{\alpha}{2}\phi + \frac{C_d}{2a}\right) \quad (20)$$
$$= \frac{1}{2}\left(u_P u_T\theta - u_P^2\right) + \frac{C_d}{2a}u_T^2$$
$$F_r \cong -\beta L \longrightarrow \frac{F_r}{ac} = \frac{-\beta}{2}\left(u_T^2\theta - u_P u_T\right) \quad (21)$$

The average aerodynamic forces and moments generated by the rotor are found by integrating the elemental forces across the blade radius (R) and over one revolution. The sideforce is omitted in this derivation. There is also a torque generated about the axis perpendicular to the rotor disc. These forces and moment are expressed as:

$$T = n_b\frac{1}{2\pi}\int_0^{2\pi}\int_0^R F_z dr\,d\psi \quad (22)$$
$$H = n_b\frac{1}{2\pi}\int_0^{2\pi}\int_0^R \left(F_x\sin\psi + F_r\cos\psi\right) dr\,d\psi \quad (23)$$
$$Q = n_b\frac{1}{2\pi}\int_0^{2\pi}\int_0^R rF_x dr\,d\psi \quad (24)$$

where n_b is the number of blades. Non-dimensional coefficients are defined as:

$$C_T = \frac{T}{\rho A(\Omega R)^2} \qquad C_H = \frac{H}{\rho A(\Omega R)^2} \quad (25)$$
$$C_Q = \frac{Q}{\rho A(\Omega R)^2 R} \qquad C_R = \frac{R}{\rho\pi R^5\Omega^2}$$

where ρ is the air density, A is the area of the rotor disc, and C_R is the rolling moment coefficient. Also, define the *rotor solidity* as the ratio of the blade area to that of the total disc:

$$\sigma = \frac{n_b c(r)R}{\pi R^2} \approx \frac{n_b c}{\pi R} \quad (26)$$

where an average chord is used to arrive at the last expression. By analogy to airplane aerodynamics C_T corresponds to span loading and the term $\frac{C_T}{\sigma}$ corresponds to lift coefficient and can be used to determine the margin to blade stall in a similar manner as C_ℓ is used to find the margin for wing stall (Ref. 18).

Rewriting Eqs. (22) - (24) in non-dimensional form results in:

$$\frac{C_T}{\sigma a} = \frac{1}{2\pi}\int_0^{2\pi}\int_0^1 \frac{F_z}{ac}dr = \frac{1}{2\pi}\int_0^{2\pi}\int_0^1 \frac{1}{2}\left(u_T^2\theta - u_P u_T\right) dr\, d\psi \tag{27}$$

$$\frac{C_Q}{\sigma a} = \frac{1}{2\pi}\int_0^{2\pi}\int_0^1 r\frac{F_x}{ac}dr\, d\psi = \frac{1}{2\pi}\int_0^{2\pi}\int_0^1 r\left[\frac{1}{2}\left(u_P u_T\theta - u_P^2\right) + \frac{C_d}{2a}u_T^2\right] dr\, d\psi \tag{28}$$

$$\begin{aligned}\frac{C_H}{\sigma a} &= \frac{1}{2\pi}\int_0^{2\pi}\int_0^1 \left(\frac{F_x}{ac}\sin\psi + \frac{F_r}{ac}\cos\psi\right) dr\, d\psi \\ &= \frac{1}{2\pi}\int_0^{2\pi}\int_0^1 \left\{\sin\psi\left[\frac{1}{2}\left(u_P u_T\theta - u_P^2\right) + \frac{C_d}{2a}u_T^2\right] \right. \\ &\left. -\beta\left[\frac{1}{2}\left(u_T^2\theta - u_P u_T\right)\right]\cos\psi\right\} dr\, d\psi\end{aligned} \tag{29}$$

where expressions for β, u_T, and u_P, and are given in Eqs. (13), (14), and (15), respectively.

The pitching and rolling moments can be found by:

$$\frac{C_{my}}{\sigma a} = -\frac{1}{2\pi}\int_0^{2\pi}\int_0^1 r\cos\psi\frac{F_z}{ac}dr\, d\psi = -\frac{1}{2}\left(-\frac{1}{6}\beta_o\mu - \frac{1}{16}\beta_{1c}\mu^2 - \frac{1}{8}\beta_{1c}\right) \tag{30}$$

$$\frac{C_{mx}}{\sigma a} = \frac{1}{2\pi}\int_0^{2\pi}\int_0^1 r\sin\psi\frac{F_z}{ac}dr\, d\psi = \frac{1}{2}\left[\frac{1}{8}\beta_{1s}\left(1-\frac{1}{2}\mu^2\right) + \frac{1}{3}\mu\left(\theta_o + \frac{3}{4}\theta_{tw} - \frac{3}{4}\lambda\right)\right] \tag{31}$$

In some derivations found in the literature, the pitch moment C_{my} integrates to zero. It does not here due to the definition of u_P in Eq. (15). If we set $u_P = \lambda$ then C_{my} will integrate to zero. The same is true for the β_{1s} term in the rolling moment expression.

Flapping Hinge Spring These expressions for the pitch and roll moments do not consider a hinge spring moment which is commonly found on multi-rotor blades that can have a *hingeless* rotor design. By including the hinge spring moment expressions for the pitch and roll moments can be derived. The hinge spring in hingeless rotors is due to the flex near the root while hinged-rotors have a dedicated mechanical hinge. For multi-rotors, the hinge spring is a virtual *structural hinge* due to the structural properties of the blade. Including the hinge spring changes the dynamics of the blade flapping and imposes an additional moment on the hinge which is transmitted to the vehicle through the rotor hub. This augments the agility of the vehicle. An articulated rotor with no hinge offset does not experience this hinge moment and aircraft moments are generated by tilting the TPP (for a helicopter).

Including the hinge spring moment, $K_\beta\beta$ where K_β is the spring coefficient, leads to a non-dimensional flapping frequency ratio defined as:

$$\lambda_b^2 = 1 + \frac{K_\beta}{I_b\Omega^2} \tag{32}$$

where $I_b = \int_0^R r^2 m(r)\, dr$ is the blade flapping moment of inertia and $m(r)$ is the linear mass density along the blade radius. The term λ_b^2 is the ratio of the flapping motion natural frequency to that of Ω. When K_β is zero, as in an articulated rotor, the ratio is unity and the blade has a flap frequency equal to Ω. In this scenario, the rotor acts like a system in resonance and has a 90^o phase lag to inputs. When $\lambda_b^2 > 1$ the blade flap frequency is slightly less than the rotational rate and the rotor responds to an input excitation with slightly less than the 90^o phase lag seen by a system in resonance. The pitch and roll moments can then be expressed as (Ref. 17):

$$\frac{C_{my}}{\sigma a} = -\frac{1}{2}\frac{\lambda_b^2 - 1}{\gamma}\beta_{1c} \tag{33}$$

$$\frac{C_{mx}}{\sigma a} = \frac{1}{2}\frac{\lambda_b^2 - 1}{\gamma}\beta_{1s} \tag{34}$$

where $\gamma = \frac{\rho a c R^4}{I_b}$ is the Lock number and represents the ratio of aerodynamic to inertial forces on the blade.

Collected Rotor Forces & Moments & Simplification

The relevant rotor forces and moments are now collected for readability and simplifications are applied to adopt the model for estimation and control approaches. The H-force and torque expressions are divided into *induced* and *profile* terms. The induced terms are those required to fly and include the terms involving the lift force. The induced terms are denoted with a subscript *i* while the profile terms have a subscript *p*.

Performing the integration in Eqs. (22) - (24), and simplifying provides the following rotor thrust, H-force, torque, pitch, and rolling moments, collected below. Note that these forces and moments are expressed in the rotor-hub frame at this stage. The first simplification is that the blade flap angles are generally small, such that multiples of flap components and higher-powers can be neglected. This has the greatest effect to simplify C_{Hi} and C_{Qi}:

$$\begin{aligned} C_T &= \frac{\sigma a}{2}\left[\frac{\theta_o}{3}\left(1+\frac{3}{2}\mu^2\right) + \frac{\theta_{tw}}{4}\left(1+\mu^2\right) - \frac{\lambda}{2}\right] \\ C_{Hi} &= \frac{\sigma a}{2}\left[\frac{\theta_o}{3}\left(\frac{3}{2}\mu\lambda - \beta_{1c}\right) + \frac{\theta_{tw}}{4}\left(\mu\lambda - \beta_{1c}\right) + \frac{3}{4}\beta_{1c}\lambda\right] \\ C_{Hp} &= \frac{\sigma C_d}{4}\mu \end{aligned} \tag{35}$$

$$C_{Qi} = \frac{\sigma a}{2}\left[\frac{1}{3}\lambda\theta_o + \frac{1}{4}\lambda\theta_{tw} + \mu\left(-\frac{1}{2}\beta_{1c}\lambda\right) - \frac{\lambda^2}{2}\right] \quad (36)$$

$$C_{Qp} = \frac{C_d\sigma}{8}\left(1+\mu^2\right)$$

$$\frac{C_{my}}{\sigma a} = -\frac{1}{2}\frac{\lambda_b^2 - 1}{\gamma}\beta_{1c}$$

$$\frac{C_{mx}}{\sigma a} = \frac{1}{2}\frac{\lambda_b^2 - 1}{\gamma}\beta_{1s}$$

The profile H-force C_{Hp} depends on the linear air velocity represented by the advance ratio μ. There are also a number of terms in the induced H-force coefficient, C_{Hi}, that involve the advance ratio and blade flap terms, revealing that there is a direct dependency of this drag term on linear air speed and blade flapping. The parasitic drag from the fuselage and non-rotating elements, proportional to the square of the air velocity, becomes dominant at higher speeds and could also be included in a model used for wind estimation.

Recall that the rotor rotational rate is part of the dimensionalization constant. Thus, the primary independent variables that could be used to model the rotor include the horizontal advance ratio μ, inflow ratio λ which includes the vertical advance ratio μ_z, rotor rotational rate Ω, and flapping angles. These observations are now included in a model for the entire vehicle that can be used in the wind estimation algorithm.

General Multi-rotor Model Structure based on First-Principles

A process model used in the wind estimation algorithm is developed in this section. This model is based on the rotor aerodynamics presented in the preceding section, with parameters identified with system identification techniques. Much of the current literature on multi-rotor dynamics modeling identifies a lumped-parameter model in linear state space form in the time domain or low-order transfer functions in the frequency domain (Refs. 23–25). Some works begin with physical principles and state or derive the forces and moments produced by a single rotor, such as (Refs. 26, 27). However, there is a gap between the rotor aerodynamics and the determination of an identifiable multi-rotor model, especially for flight conditions beyond hover. A hypothesized model structure of a multi-rotor in forward flight using the results from the individual rotor analysis is presented. By lumping constant parameters, and adding airframe-specific effects, parameters of the model can be identified from flight or simulator data. The approach mostly resembles that from (Ref. 27).

Rotor in Forward Flight Consider a n_b-blade rotor of radius R with an angular speed of Ω $\frac{\text{rad}}{\text{s}}$ in steady forward flight with airspeed V at some incidence angle, i. The thrust (T), torque (Q), hub force (H), and rolling moment (R) produced by this rotor can be expressed as Eqs. (36) and (37).

The inflow velocity can be expressed with Eq. (12) using momentum theory assuming the disk is at zero angle-of-incidence moving horizontally. To simplify the dependence on V, notice inflow can be well-approximated by a quadratic polynomial. However, this still leads to high order terms in the model such as V^4, which are not easily identified from flight data. Therefore, an additional simplification is made to approximate the inflow velocity to be linear in airspeed:

$$v \approx v_0 + C_{v_1} V \quad (37)$$

which is the case in momentum theory of ascending flight. Here, v_0 is found by evaluating Eq. (12) at zero airspeed (hover).

Without loss of generality, let $n_b = 1$. Collecting terms yields the following for the thrust coefficient, where the parameters have been explicitly identified:

$$C_T = \underbrace{\left(\frac{ac\left(\frac{\theta_0}{6} + \frac{\theta_{tw}}{8}\right)}{\pi R}\right)}_{C_{T_0}} + \underbrace{\left(\frac{-acC_{v_1}}{4\pi R}\right)}_{C_{T_\mu}}\frac{V}{\Omega R} + \quad (38)$$

$$\underbrace{\left(\frac{ac\left(\frac{\theta_0}{4} + \frac{\theta_{tw}}{8}\right)}{\pi R}\right)}_{C_{T_{\mu^2}}}\frac{V^2}{\Omega^2 R^2} + \underbrace{\left(\frac{-ac}{4\pi R}\right)}_{C_{T_v}}\frac{v_0}{\Omega R} + \underbrace{\left(\frac{ac}{4\pi R}\right)}_{C_{T_{\mu_z}}}\frac{w}{\Omega R}$$

This expansion is performed for each of the force and moment coefficients. Rewriting in terms of lumped parameters yields:

$$C_T = C_{T_0} + C_{T_\mu}\mu + C_{T_{\mu^2}}\mu^2 + C_{T_v}\frac{v_0}{\Omega R} + C_{T_{\mu_z}}\mu_z \quad (39a)$$

$$C_Q = C_{Q_0} + C_{Q_\mu}\mu + C_{Q_{\mu^2}}\mu^2 + C_{Q_{\mu v}}\mu\frac{v_0}{\Omega R} \quad (39b)$$

$$+ C_{Q_{\mu\mu_z}}\mu\mu_z + C_{Q_v}\frac{v_0}{\Omega R} + C_{Q_{v^2}}\frac{v_0^2}{\Omega^2 R^2} + C_{Q_{\mu_z}}\mu_z$$

$$+ C_{Q_{\mu_z^2}}\mu_z^2 + C_{Q_{\mu_z v}}\mu_z\frac{v_0}{\Omega R} \quad (39c)$$

$$C_H = C_{H_\mu}\mu + C_{H_{\mu^2}}\mu^2 + C_{H_{\mu v}}\mu\frac{v_0}{\Omega R} + C_{H_{\mu\mu_z}}\mu\mu_z \quad (39d)$$

$$C_R = C_{R_\mu}\mu + C_{R_{\mu^2}}\mu^2 + C_{R_{\mu v}}\mu\frac{v_0}{\Omega R} + C_{R_{\mu\mu_z}}\mu\mu_z \quad (39e)$$

Multi-rotor Definitions and Assumptions Although it is possible to identify a model summing all the rotor forces and moments, the extensive, high-order, nonlinear model structure would make parameter identification challenging. Instead, the rotor force and moment equations help to hypothesize a set of candidate regressors, including regressors specific to airframe aerodynamics. Further, instead of treating individual rotor speed as the system input, the following motor mixing is used:

$$\begin{bmatrix}\delta t\\ \delta a\\ \delta e\\ \delta r\end{bmatrix} = \mathbf{M_{ix}}\begin{bmatrix}\Omega_1^2\\ \Omega_2^2\\ \vdots\\ \Omega_{N_{rot}}^2\end{bmatrix} \quad (40)$$

where $\mathbf{M_{ix}}$ is determined by the geometry of the multi-rotor with N_{rot} rotors. The system inputs can then be expressed in terms of δt for throttle or collective, δa for aileron, δe for elevator, and δr for rudder. Additionally, to capture terms that appear such as $(-\Omega_1 + \Omega_2 + \Omega_3 - \Omega_4)$, define the notation:

$$\begin{bmatrix} \sqrt[\Omega]{\delta t} \\ \sqrt[\Omega]{\delta a} \\ \sqrt[\Omega]{\delta e} \\ \sqrt[\Omega]{\delta r} \end{bmatrix} := \mathbf{M_{ix}} \begin{bmatrix} \Omega_1 \\ \Omega_2 \\ \vdots \\ \Omega_N \end{bmatrix} \tag{41}$$

For example, a quadrotor in a symmetric "X" configuration may have the mixing:

$$\begin{bmatrix} \delta t \\ \delta a \\ \delta e \\ \delta r \end{bmatrix} = \begin{bmatrix} 1 & 1 & 1 & 1 \\ -1 & -1 & 1 & 1 \\ 1 & -1 & -1 & 1 \\ 1 & -1 & 1 & -1 \end{bmatrix} \begin{bmatrix} \Omega_1^2 \\ \Omega_2^2 \\ \Omega_3^2 \\ \Omega_4^2 \end{bmatrix} \tag{42}$$

Furthermore, this problem presents some nuances that do not appear with a single rotor. First, the rotor forces and moments are now defined in the body frame. Therefore, the rotor side force coefficient, C_Y, and pitching coefficient, C_P, are no longer zero. Thus, the direction of the velocity vector now matters - not just the airspeed. The advance ratios that appear in Eq. (40) are not simply defined by airspeed at the aircraft's CG. Instead, one must use the component of the velocity vector that influences the force or moment in question plus the contribution of the velocity at the rotor hub due to the vehicle angular velocity. However, this approach gives a complicated structure where the virtual actuators cannot fully replace the rotor speeds. Therefore, the following assumption and remarks are made:

Assumption 1 *The vehicle angular velocity contributes to the local advance ratios which define the rotor forces and moments. These effects can be approximated by additional terms in each force/moment equation that depend on the vehicle angular velocity.*

Remark 1 *The velocity vector used to determine the airspeed that defines μ in C_T and C_Q is the projection of $\boldsymbol{v}$ onto the $\boldsymbol{b}_1 - \boldsymbol{b}_2$ plane (i.e. $\sqrt{u^2+v^2}$).*

Remark 2 *The velocity vector used to determine the airspeed that defines μ in C_H, C_Y, C_R, and C_P is the component of $\boldsymbol{v}$ along the axis of that force or moment arm, respectively (i.e. u for C_H and C_R; v for C_Y and C_P).*

Multi-rotor Forces and Moments A 6 degree-of-freedom (DOF) model structure is now postulated taking inspiration from these results. This model structure is given with system identification from flight and/or simulation data in mind (as opposed to wind tunnel and rotor data). Furthermore, terms in this model structure can be removed or added through a model structure determination approach, such as multivariate orthogonal function modeling or step-wise regression (Ref. 21).

Consider a quadrotor in a symmetric "X" configuration as pictured in Figure 10 with the motor mixing defined in Eq. (43). The following derivation considers four equally spaced, identical rotors; however, the final result is agnostic to the number of rotors. In general, the force of the i-th rotor expressed in the body frame is:

$$\boldsymbol{F}_i = \rho R^4 \Omega_i^2 \begin{bmatrix} -C_{H_i} \\ C_{Y_i} \\ -C_{T_i} \end{bmatrix} \tag{43}$$

where C_{Y_i} is the hub force in the body y direction. Similarly, the moment about the aircraft's center of gravity produced by the i^{th} rotor is

$$\boldsymbol{M}_i = \varepsilon_i \rho R^5 \Omega_i^2 \begin{bmatrix} -C_{R_i} \\ C_{P_i} \\ -C_{Q_i} \end{bmatrix} + \boldsymbol{r}_i \times \boldsymbol{F}_i \tag{44}$$

where C_{P_i} is the pitching moment of the rotor and $\varepsilon_i \in \{-1, +1\}$ represents the rotor direction. For example, the moment due to rotor number one (geometry defined in Figure 10) is:

$$\boldsymbol{M}_1 = \rho R^4 \Omega_1^2 \left(-R \begin{bmatrix} -C_{R_1} \\ C_{P_1} \\ -C_{Q_1} \end{bmatrix} + \begin{bmatrix} -bC_{T_1} + hC_{Y_1} \\ bC_{T_1} + hC_{H_1} \\ b(C_{H_1} + C_{Y_1}) \end{bmatrix} \right) \tag{45}$$

Summing the forces and moments for all four rotors, substituting the virtual actuator definitions from Eq. (43) and (42), and using Assumption 1, results in Eq. (47), where b is the radial distance from the CG to each rotor hub, $V = \sqrt{u^2+v^2+w^2}$, and $\sqrt{\delta t}$ can be thought of as a rotor speed magnitude.

The parameters highlighted in red were dropped from the final model structure as explained in the following section. A non-dimensional form of these equations can also be derived. There are no airframe-specific drag terms in the above force and moment equations. It is assumed that such effects are lumped in with other identified parameters. For this reason, the identified C_{H_μ} and the X and Y force equations may differ.

System Identification Results

Although the state trajectories of a multi-rotor may be open-loop unstable, e.g., near hover, an open-loop model is identified from closed-loop flight data. A high-fidelity multi-rotor simulation developed at NASA (Ref. 20) is used to generate surrogate flight data. The inputs to the multi-rotor from the controller are motor throttle commands as a percentage of maximum motor speed. Due to the structure of the simulator, an excitation signal was injected at the throttle commands to each motor. The excitation input is a 4-axis phase-optimized orthogonal multisine signal for the virtual actuator multiplied by the pseudo-inverse of $\mathbf{M}_{\text{ix}}$, thus retaining orthogonality and decorrelation of the inputs in the input signal. The optimized

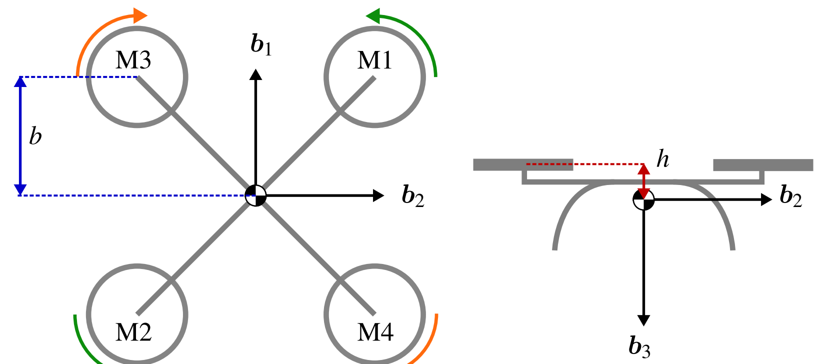

Figure 10. Quadrotor configuration

orthogonal multisine excitation signal is designed as a perturbation command with wideband frequency content over a desired frequency range. It features nearly uniform power over the selected frequency band and provides decorrelated input signals due to the orthogonality property. Phase shifts for the sinusoidal components of each input are optimized to achieve low peak-to-peak amplitude and high input energy content for the sum of sinusoids. Amplitudes of the individual sinusoidal components can be chosen to achieve a specific power distribution (Ref. 21).

$$X = \rho\pi R^2 u\Big(C_{X_{H_\mu}} R\sqrt[\Omega]{\delta t} + N_{\mathrm{rot}}\Big(C_{X_{H_{\mu 2}}} u\,\mathrm{sign}(u) + C_{X_{H_{\mu\mu_z}}} w + C_{X_{H_{\mu v}}} v_0\Big)\Big) \tag{46a}$$

$$Y = \rho\pi R^2 v\Big(C_{Y_{H_\mu}} R\sqrt[\Omega]{\delta t} + N_{\mathrm{rot}}\Big(C_{Y_{H_{\mu 2}}} v\,\mathrm{sign}(v) + C_{Y_{H_{\mu\mu_z}}} w - C_{Y_{H_{\mu v}}} v_0\Big)\Big) \tag{46b}$$

$$Z = -\rho\pi R^2\Big(C_{Z_{T_0}} R^2\delta t + C_{Z_{T_v}} R v_0\sqrt[\Omega]{\delta t} + C_{Z_{T_\mu}} R\sqrt{u^2+v^2}\sqrt[\Omega]{\delta t} + C_{Z_{T_{\mu_z}}} R w\sqrt[\Omega]{\delta t} + N_{\mathrm{rot}} C_{Z_{T_{\mu 2}}}(u^2+v^2)\Big) \tag{46c}$$

$$\begin{aligned}\mathscr{L} = \rho\pi R^2\Big(&bR\Big(C_{l_{T_0}} R\delta a - C_{l_{T_v}} v_0\sqrt[\Omega]{\delta a} + C_{l_{T_\mu}}\sqrt{u^2+v^2}\sqrt[\Omega]{\delta a} + C_{l_{T_{\mu_z}}} w\sqrt[\Omega]{\delta a}\Big) + C_{l_{R_\mu}} R^2 u\sqrt[\Omega]{\delta r} + C_{l_{H_\mu}} hRv\sqrt[\Omega]{\delta t} + \\ &N_{\mathrm{rot}} hv\Big(C_{l_{H_{\mu 2}}} v\,\mathrm{sign}(v) - C_{l_{H_{\mu\mu_z}}} w + C_{l_{H_{\mu v}}} v_0\Big) + C_{l_{p,\delta t}} b^2 p\sqrt{\delta t} + C_{l_p}\frac{b}{v_0}V^2 p\Big)\end{aligned} \tag{46d}$$

$$\begin{aligned}\mathscr{M} = \rho\pi R^2\Big(&bR\Big(C_{m_{T_0}} R\delta e + C_{m_{T_v}} v_0\sqrt[\Omega]{\delta e} + C_{m_{T_\mu}}\sqrt{u^2+v^2}\sqrt[\Omega]{\delta e} - C_{m_{T_{\mu_z}}} w\sqrt[\Omega]{\delta e}\Big) + C_{m_{R_\mu}} R^2 v\sqrt[\Omega]{\delta r} - C_{m_{H_\mu}} hRu\sqrt[\Omega]{\delta t} + \\ &N_{\mathrm{rot}} hu\Big(C_{m_{H_{\mu 2}}} u\,\mathrm{sign}(u) + C_{m_{H_{\mu\mu_z}}} w - C_{m_{H_{\mu v}}} v_0\Big) + C_{m_{q,\delta t}} b^2 q\sqrt{\delta t} + C_{m_q}\frac{b}{v_0}V^2 q\Big)\end{aligned} \tag{46e}$$

$$\begin{aligned}\mathscr{N} = \rho\pi R^2\Big(&C_{n_{Q_0}} R^3\delta r + C_{n_{Q_v}} R^2 v_0\sqrt[\Omega]{\delta r} + C_{n_{Q_\mu}} R^2\sqrt{u^2+v^2}\sqrt[\Omega]{\delta r} + C_{n_{Q_{\mu_z}}} R^2 w\sqrt[\Omega]{\delta r} + bC_{n_{H_\mu}}\Big(u\sqrt[\Omega]{\delta a} + v\sqrt[\Omega]{\delta e}\Big) + \\ &C_{n_{r,\delta t}} b^2 r\sqrt{\delta t} + C_{n_r}\frac{b}{v_0}V^2 r\Big)\end{aligned} \tag{46f}$$

The model structure of Eq. (47) is hypothesized for general flight conditions and the excitation signal is designed to cover a range of rates and attitudes. Therefore, a 3-axis low-frequency multisine (0.001 to 0.01 Hz frequency range) is added to the motor excitation signal to command reference roll, pitch, and yaw attitudes. The effects of using this reference signal in conjunction with the multisine excitation signal can be seen in Figure 11. In this figure, the high-frequency content (solid lines) results from the excitation signal commanded to the motors and the low-frequency content (dashed lines) maneuvers the vehicle through a range of operating conditions. This approach is similar to the one presented in (Ref. 28) where a fixed-wing aircraft was commanded to maneuver through a range of angles-of-attack while optimized multisine signals created information rich input-output data used to generate a global nonlinear model.

A single maneuver consisting of 5 seconds of hover and 2 minutes of excitation was used to identify the parameters in (47). Step-wise regression was employed to refine the model structure (Ref. 21). The step-wise regression results showed all parameters to be statistically significant; however, the parameters highlighted in red had large standard errors and 95% confidence intervals crossing zero. These regressors were removed from the model. Additionally, step-wise regression revealed that additional bias terms for each axis were small.

Equation-error parameter estimation was used to estimate the remaining parameters (Refs. 21, 22). The results of the model fit are tabulated in Table 1 for each force and moment. The

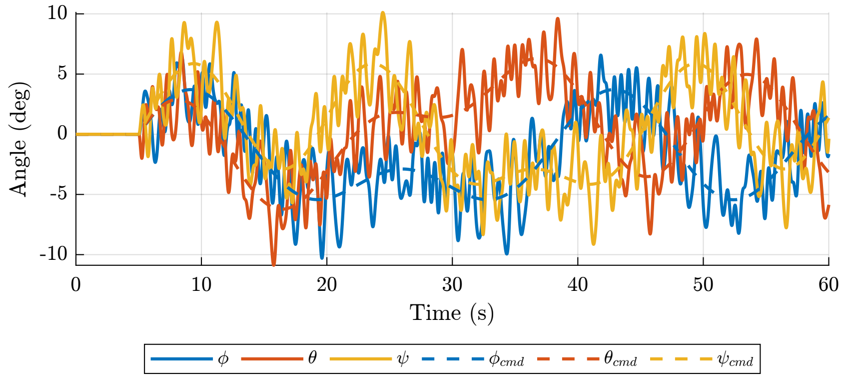

Figure 11. Excited attitude

coefficient of determination, R^2 is used to quantify the accuracy of the identified model. The coefficient of determination provides a proportional sum-of-squares measure of the model fit and indicates the percentage of the variation in the observations explained by the model. The square of the model fit error $s^2 = (\sum_{i=1}^{N}[z(i) - \hat{y}(i)]^2)/(N - n_p)$ is also used to evaluate the accuracy of the identified model. Here, $z(i)$ is the measurement at the i^{th} time step, $\hat{y}(i)$ is the estimated output at this time, N is the number of time steps, and n_p is the number of parameters. The s^2 metric is the square of the average distance between the estimated and measured values, reported in the physical units squared.

Table 1. Equation error results

Axis	R^2(%)	s^2
X	99.5	2.1972e-04
Y	88.7	1.8476e-04
Z	95.0	2.0359e-02
$\mathscr{L}$	92.0	5.9820e-04
$\mathscr{M}$	94.4	4.7276e-04
$\mathscr{N}$	54.3	1.3082e-02

The estimated parameter values and 95% confidence intervals are given in the appendix in Table 5. The known constant parameters used in Eq. (47) are given in Table 2.

Table 2. Vehicle parameters

N_{rot}	$\rho\ \left[\frac{\text{slug}}{\text{ft}^3}\right]$	R[ft]	b[ft]	$g\ \left[\frac{\text{ft}}{\text{s}^2}\right]$	$v_0\ \left[\frac{\text{ft}}{\text{s}}\right]$
4	0.002377	0.5833	0.6681	32.174	17.43

The model fit on this training maneuver is shown in Figure 12a. The parameters were identified using training data spanning the region described in Table 3, approximating the valid domain of this model.

The R^2 and s^2 metrics indicated the accuracy of the identified model on the training data, but do not provide any predictive information. The model's predictive capability, tabulated in Table 4, is evaluated using Theil's inequality coefficient:

Table 3. Model domain

Variable	Units	5th percentile	95th percentile
u	ft/s	-12.56	11.87
v	ft/s	-12.82	13.45
w	ft/s	-2.617	1.547
p	rad/s	-0.422	0.421
q	rad/s	-0.421	0.421
r	rad/s	-0.417	0.417
δt	$(\frac{\text{rad}}{\text{s}})^2 \times 10^5$	4.157	8.206
δa	$(\frac{\text{rad}}{\text{s}})^2 \times 10^5$	-0.503	0.526
δe	$(\frac{\text{rad}}{\text{s}})^2 \times 10^5$	-0.512	0.544
δr	$(\frac{\text{rad}}{\text{s}})^2 \times 10^5$	-0.796	0.796
Ω_i	rad/s	318.2	464.6

$$\text{TIC} = \frac{\sqrt{\frac{1}{N}(\boldsymbol{z} - \hat{\boldsymbol{y}})^\top(\boldsymbol{z} - \hat{\boldsymbol{y}})}}{\sqrt{\frac{1}{N}\boldsymbol{z}^\top\boldsymbol{z}} + \sqrt{\frac{1}{N}\hat{\boldsymbol{y}}^\top\hat{\boldsymbol{y}}}} \tag{47}$$

and normalized root mean squared error (NRMSE):

$$\text{NRMSE} = \frac{1}{\text{range}(\boldsymbol{z})}\sqrt{\frac{(\boldsymbol{z} - \hat{\boldsymbol{y}})^\top(\boldsymbol{z} - \hat{\boldsymbol{y}})}{N}} \tag{48}$$

where $\boldsymbol{z}$ is a column vector of measurements, $\hat{\boldsymbol{y}}$ is a column vector of estimated outputs, and N is the number of data points. For both TIC and NRMSE, 0 indicates a perfect fit. Theil's inequality coefficient is useful in comparing the results with other models or data sets, as it is normalized between 0 and 1. In air vehicle system identification a value less than 0.3 is often considered sufficient (Ref. 29). The NRMSE is used to give a measure of the predictive ability of the model against independent data. The normalization makes comparison between axes straightforward.

The identified model is validated against an independent maneuver excited by a different multisine signal and attitude reference signal, as seen in Figure 12b. The identified model shows desirable predictive capability for the modeled forces and moments with the exception of the yaw moment, which exhibits increased mismatch relative to the other axes. This

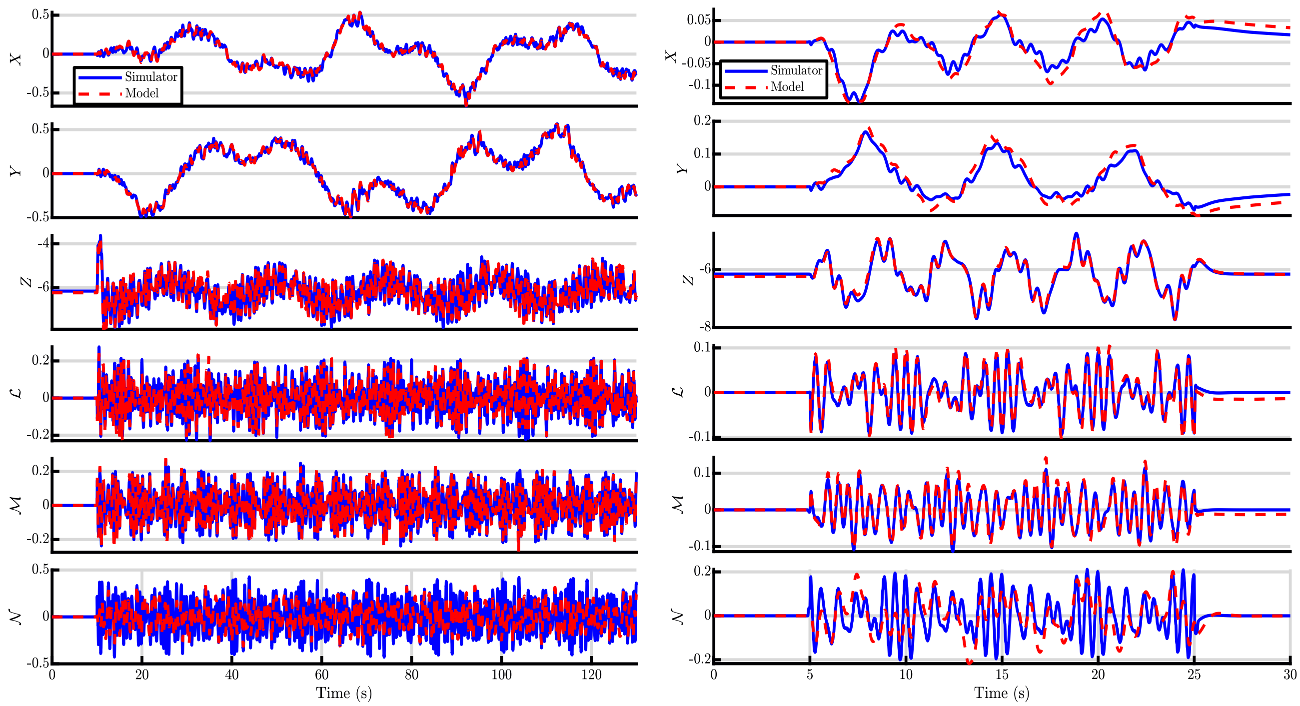

(a) Model fit

(b) Force and Moment validation

Figure 12. Nonlinear model fit and validation

discrepancy could be resolved with additional modeling data. It is also possible that, since the vehicle is underactuated, it does not possess sufficient control authority to track commands in all six axes simultaneously and an improved fit could be found by collecting modeling data with an independent yaw axis maneuver. This can be investigated in future work.

Table 4. Model predictive metrics

Axis	TIC	NRMSE
X	0.1676	0.0750
Y	0.1574	0.0809
Z	0.0060	0.0250
$\mathscr{L}$	0.1409	0.0568
$\mathscr{M}$	0.1370	0.0512
$\mathscr{N}$	0.4588	0.1675

WIND ESTIMATOR

This section discusses development of the wind estimator, composed of two primary components: 1) the process and measurement models and 2) the estimator algorithm. A candidate process model structure based on rotor blade element theory and an efficient method to determine an identified model based on this structure is presented in the prior section. A Bayesian wind estimation algorithm is developed to estimate the 3D wind vector using standard autopilot sensors, such as GNSS, IMU, and rotor speed data. In the case of GPS-denied operations, position and inertial velocity based on visual-inertial odometry (VIO), SLAM, or other approaches can be used. An unscented Kalman filter (UKF) is used to estimate wind states in a recursive manner. For linear systems with independent Gaussian noise and other assumptions, the linear Kalman filter can be used to optimally estimate the state. For nonlinear systems the UKF variant is preferred. The literature demonstrates that the UKF is generally more accurate and more robust to large initialization errors and system nonlinearities than the extended Kalman filter. It is often easier to implement as well since Jacobians need not be derived (Refs. 30–32).

The process and measurements models should be constructed in a form that exposes all the estimated states, particularly the wind states. The process model will follow the discussion presented in the prior section. A compact version of the model is presented here, tailored for implementation with the UKF estimator. Recall, that each rotor generates a thrust T, H-force H (or rotor drag), rotor torque Q_R, pitching moment $\mathscr{M}_{\mathscr{R}}$, and rolling moment $\mathscr{L}_{\mathscr{R}}$ summarized in Eqs. (36) and (37). These forces and moments are expressed in the *hub-wind* frame which is the rotor hub frame rotated about the vertical axis so the x_h axis points toward to relative wind vector. Define $\boldsymbol{R}^b_{hw}$ to be the rotation vector from the hub wind frame to the body frame. Then the rotor forces are expressed in the body frame with a superscript b as $\left[F^b_{R,x}, F^b_{R,y}, F^b_{R,z}\right]^T$. The vehicle studied in this project has canted rotor arms, so the thrust and H-force will have components in each body-frame axis. Inertial accelerations are expressed in the body frame as $\dot{\boldsymbol{v}}_i^b$ with inertial winds expressed in the body frame as $\boldsymbol{w}_i^b$, where $i \in \{x,y,z\}$ denotes the axis:

$$\begin{aligned}\boldsymbol{f}(\boldsymbol{x},\boldsymbol{u}) &= \begin{bmatrix}\dot{v}_x^b\\ \dot{v}_y^b\\ \dot{v}_z^b\end{bmatrix} \\ &= \boldsymbol{R}_I^b\begin{bmatrix}0\\0\\g\end{bmatrix} + \boldsymbol{\omega}\times\boldsymbol{v^b} + \boldsymbol{R}_h^b\begin{bmatrix}H\\0\\T\end{bmatrix} + \begin{bmatrix}F_{A,x}\\F_{A,y}\\F_{A,z}\end{bmatrix}\end{aligned} \tag{49}$$

where $F_{A,i}$ are the aerodynamic forces from the fuselage. The wind effects are made clear by expanding the rotor forces expressed in the body-frame which are the dominant forces, along with gravity, unless the vehicle reaches high advance ratio flight where the drag of the fuselage becomes important.

The j^{th} rotor forces expressed in the body frame are shown in Eq. (51) where $v_i^{b,j}$ is the rotor hub velocity of the j^{th} rotor in the body-frame, and K_{CHi} and K_{CTi} are the contributions from the H-force and thrust force in the body (x,y,z) frame. These are the same equations as those presented earlier but rewritten to expose the wind components. The H-force and thrust are also dependent on the airspeed vector. The function for the moments is given by Eq. (4).

$$F_{R,x}^{b,j} = \rho A\left(R\Omega_j\right)^2\left[-K_{CHx}C_{H_j}^b\frac{v_x^{b,j}+w_x^b}{\sqrt{\left(v_x^{b,j}+w_x^b\right)^2+\left(v_y^{b,j}+w_y^b\right)^2}} - K_{CTx}C_{T_j}^b\right] \tag{50a}$$

$$F_{R,y}^{b,j} = \rho A\left(R\Omega_j\right)^2\left[-K_{CHy}C_{H_j}^b\frac{v_y^{b,j}+w_y^b}{\sqrt{\left(v_x^{b,j}+w_x^b\right)^2+\left(v_y^{b,j}+w_y^b\right)^2}} - K_{CTy}C_{T_j}^b\right] \tag{50b}$$

$$F_{R,z}^{b,j} = \rho A\left(R\Omega_j\right)^2\left[-K_{CHz}C_{H_j}^b\frac{v_z^{b,j}+w_z^b}{R\Omega} - K_{CTz}C_{T_j}^b\right] \tag{50c}$$

One possible process model for the wind dynamics is a random walk model (Brownian motion) driven by a Gaussian noise term. Let the airspeed states be defined as $\boldsymbol{V_a^b} = \boldsymbol{x}^b + \boldsymbol{w}^b$, producing the following process model:

$$\dot{\boldsymbol{V}}_a^b = f(\boldsymbol{x},\boldsymbol{u}) + \dot{\boldsymbol{w}}^b \tag{51}$$

$$\mathbf{M} = I_b\dot{\boldsymbol{\omega}}_b + \boldsymbol{\omega}_b\times I_b\boldsymbol{\omega}_b = \mathbf{M}_A + \mathbf{M}_R \tag{52}$$

$$\dot{\boldsymbol{w}}^b = \mathbf{0} + \mathscr{Q}_w \tag{53}$$

where $\mathscr{Q}_w$ is a Gaussian process noise term. The measurements include inertial position and velocity, rotational rates, Euler angles, rotor speed, and accelerations. The estimator is then formulated to estimate the states in Eq. (52) - (54).

Wind Estimation Demonstration

This section presents results of the wind estimator under two operating scenarios, briefly described below.

- **Scenario 1**: The vehicle is commanded to hover while subjected to steady winds that change direction at a simulation time of 23 seconds. Turbulent winds based on the Kaimal spectra are added to the steady winds. The steady winds transition from $[10,0,0]^T$ to $[7.07,7.07,3]^T$ at 23 seconds.
- **Scenario 2**: The vehicle is commanded to fly to different waypoints and collect data at each waypoint. Steady and turbulent winds buffet the vehicle with the steady wind component set to $[10,0,0]^T$.

For these scenarios, realistic noise is added to the measured values based on representative MEMS hardware present on modern autopilot systems. Process noise is also added to the simulation model used to generate the data used to evaluate the wind estimator. In the following discussion, W_x, W_y, W_z represent the inertial winds in the wind frame described in Figure 6b. The mean estimate is shown as a solid line with a $\pm 2\sigma$ confidence interval (CI) shown as a shaded region. The true wind value is shown as a dashed green line. Turbulent winds are added to steady-wind signals based on an exact non-causal filtering approach using a modified Kaimal spectrum to produce the turbulence signals. The Kaimal spectrum is often used in the wind energy and civil engineering communities to accurately produce turbulence in the atmospheric surface layer (ASL), which extends from the surface to approximately 200 meters above ground level (AGL). A modified Kaimal spectrum extends the height to expected operating conditions for this program. The modified Kaimal spectrum has been found to more accurately represent observed turbulence at lower altitude conditions compared to von Karman and Dryden spectra (Ref. 33).

Results for Scenario 1 are presented in Figure 13 and show desirable performance. The estimator tracks the turbulent winds with a slight degradation in the vertical channel.

Scenario 2 presents flight more representative of an operational mission. As shown in Figure 14, the vehicle hovers for approximately 5 seconds at the initial position and then transitions to a waypoint 100 feet north of the initial position. Once capturing this waypoint, the vehicle loiters for 10 seconds and then transitions to a third waypoint. This represents

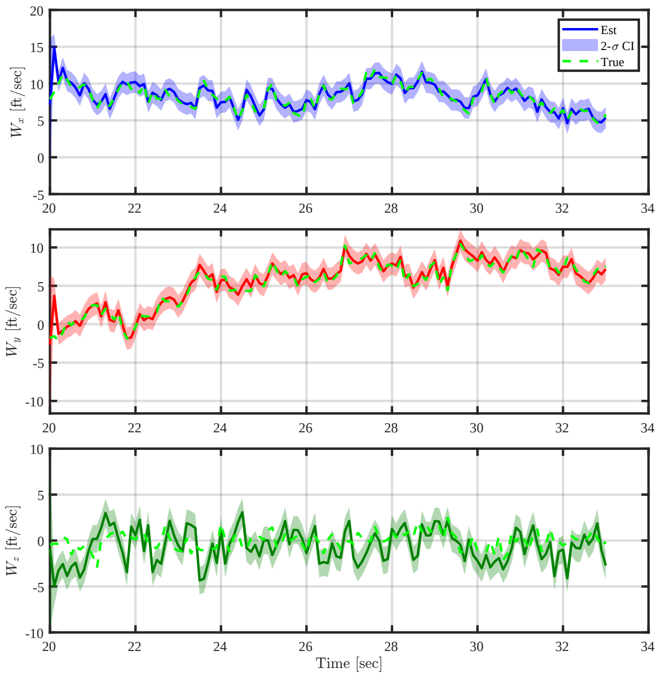

Figure 13. Wind estimation for Scenario 1: vehicle at a near hover with steady and turbulent winds active. The steady wind component changes direction at 23 seconds.

maneuvering typical of a mission and desired wind estimates are found, displayed in Figure 15. There is a mild increase in error compared to the first scenario; however, the estimates are sufficiently accurate to determine mean ambient wind conditions necessary to assist in source localization strategies.

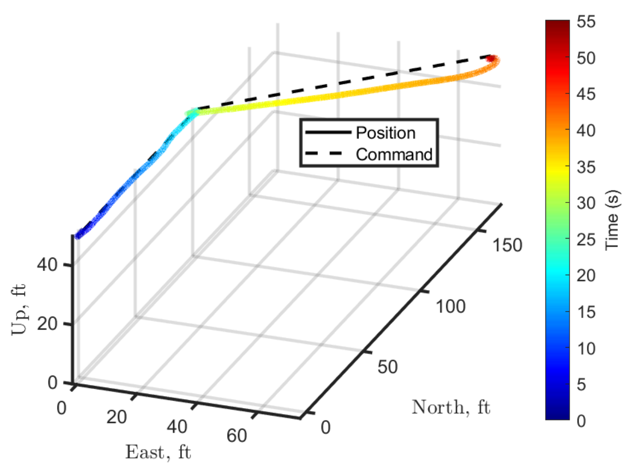

Figure 14. Wind estimation with Scenario 2: the vehicle hovers at the initial condition and then transitions to two additional waypoints, loitering at each waypoint for 10 seconds. Steady and turbulent winds are active.

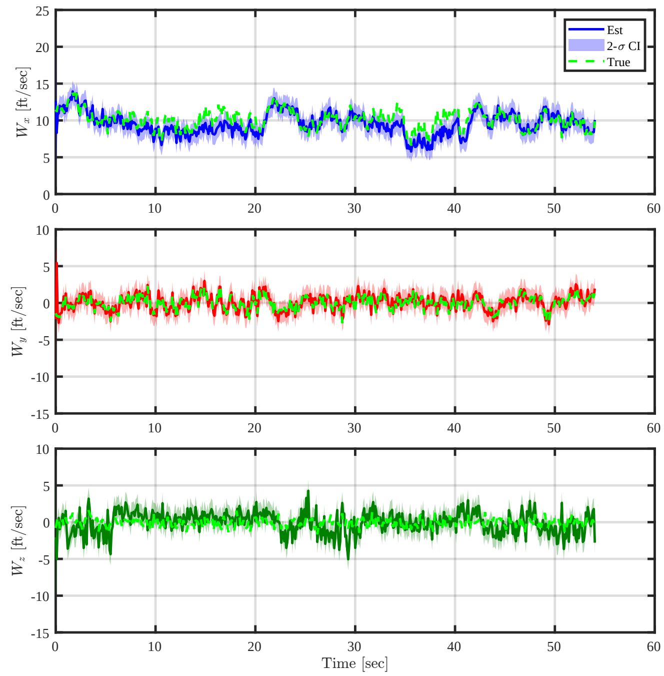

Figure 15. Wind estimates for scenario 2

SOURCE LOCALIZATION USING ESTIMATED WINDS

This section presents approaches to utilize the wind estimator with different source localization techniques. Two techniques are considered: 1) an anemotaxic approach where the vehicle estimates the upwind direction and flies in that direction, and 2) a biologically-inspired search algorithm mimicking a dung beetle. The simulation environment utilized in these experiments includes three primary components: 1) a high-fidelity NASA multi-rotor vehicle model (Ref. 20), 2) the Quick Urban and Industrial Complex (QUIC) Dispersion Modeling System (Refs. 34–36), a tool used to generate realistic wind and plume dispersion in complex environments, and 3) a chemical sensor. Basic autopilot control is used to stabilize the vehicle and execute waypoint tracking.

Anemotaxis Source Localization using Estimated Wind Direction

The approach employed in this section mimics the surge-casting behavior of the silkworm moth by commanding the vehicle to fly in an upwind direction. The wind environment consists of steady and turbulent winds. The true direction of the steady winds changes every 10 seconds as depicted in Figure 16. This figure shows both the truth wind direction with the signal "Steady Wind Heading" and the estimated wind direction with the signal "Heading Cmd", which is also the commanded heading for the vehicle.

The wind estimator estimates a 3D wind vector and the horizontal wind direction is found with the $\hat{W}_x$ and $\hat{W}_y$ wind components. Since the primary interest is in the low-frequency wind component, i.e., the vehicle should not sporadically

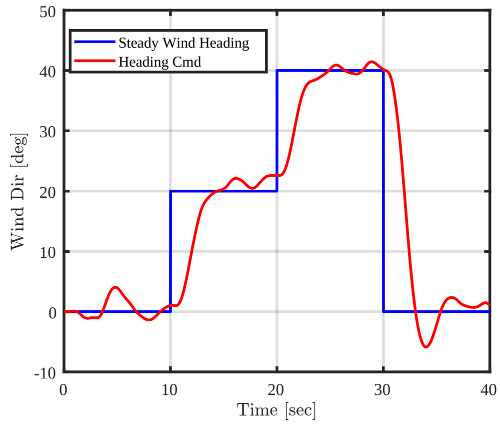

Figure 16. True and estimated changes to the wind direction

change heading based on turbulence, the estimated wind direction is filtered with a low-pass Butterworth filter. This removes the high-frequency content from the signal and generates a moving-average of the low-frequency content. The cutoff frequency of the filter can be arbitrarily set for the operating environment. Also recall that the estimated wind direction does include turbulent effects and so the match to the steady-state wind direction has acceptable error.

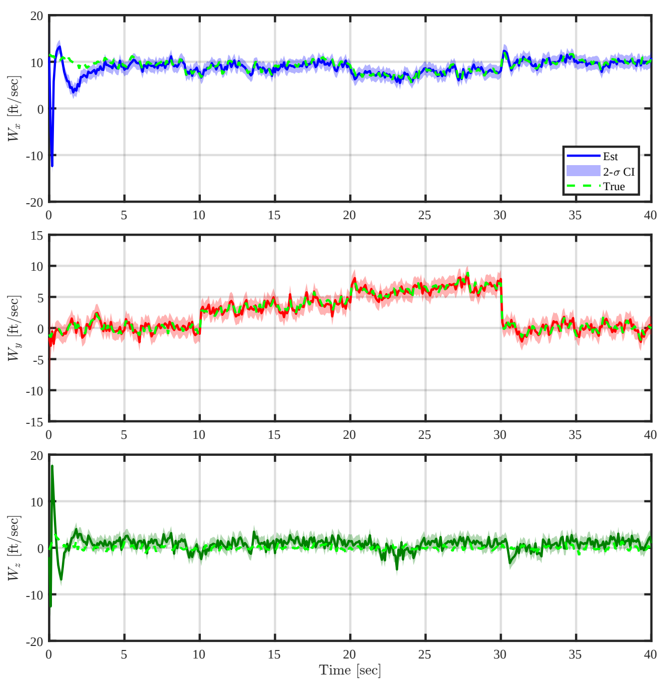

Figure 17. Estimated wind components with changing wind direction

The estimated wind components for this maneuver are shown in Figure 17 which shows a desirable comparison with the true winds. The initial spikes in the estimated signals are caused by initializing the filter with no prior information, i.e. the initial wind estimate is set to zero with large covariance. The flight path of the vehicle is shown in Figure 18 where it can be observed that the vehicle alters heading at approximately 10 second intervals to follow the change in wind direction. The solid multi-colored line shows the vehicle's position over time and the dashed line shows the commanded position. The error in position tracking is caused by the effects of the winds.

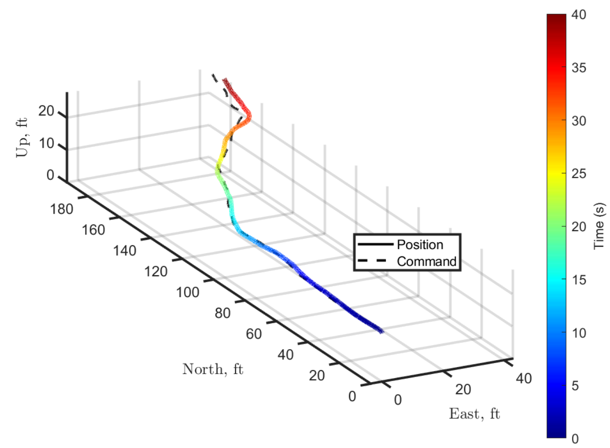

Figure 18. Flight path of vehicle flying upwind in changing wind direction

Source Localization in an Urban Setting

This section presents the results of integrating the wind estimator with a source localization approach inspired by the dung beetle. As described in (Ref. 8), "Upon detecting the odour it [the dung beetle] zigzags diagonally across the plume in an upwind direction turning back each time it leaves the edge of the plume. When the odour plume ends, as it does immediately above the cow pat, the beetle flies down and usually lands on or near its goal."

A version of the dung beetle search strategy was implemented using the UKF wind estimator to provide estimates of the 3D wind vector and wind direction. The vehicle is commanded to navigate towards the source in an urban environment. Wind and chemical concentration information are simulated with QUIC. The winds are created with a logarithmic profile with a magnitude of 7 (m/s) at a reference height of 10 (m) and a direction of 45^o. Figure 19 portrays the scenario where there are six buildings represented by gray patches. The plume concentration is shown as the shaded regions with higher concentration levels depicted with yellow and green regions, while lower concentration levels are purple in color. The UAS is initialized at (340, 30) and the flight trajectory is shown as a black line. During flight, the UAS encounters a turbulent plume and wind conditions.

The wind estimator performance is shown in Figure 20 and shows excellent performance for the x- and y- axes with a

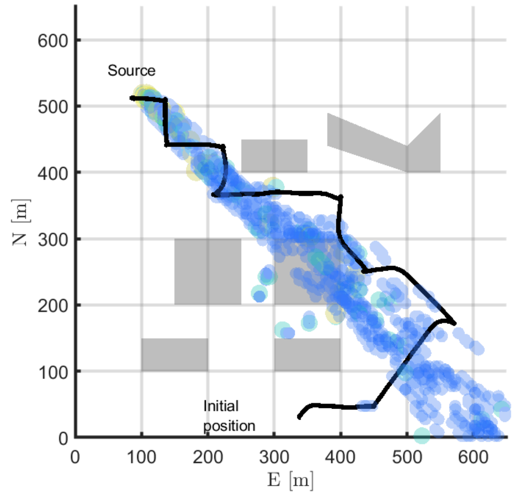

Figure 19. Wind estimation and source localization in an urban setting

slight bias in the vertical axis, which could be resolved in future work with additional filter tuning. However, estimating the horizontal wind direction and magnitude are the primary concerns for this project.

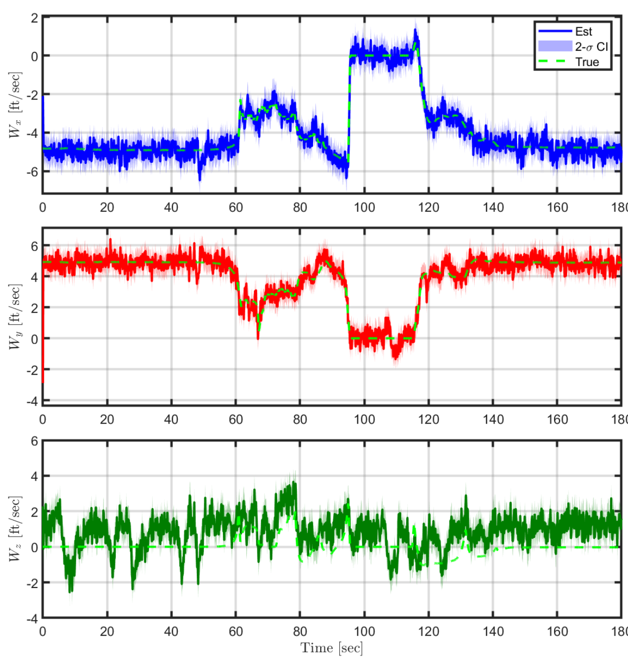

Figure 20. Wind estimator performance for an urban mission

CONCLUSIONS

This paper discussed a methodology to sense ambient wind conditions to assist in localizing the source of a released agent using small unmanned aerial systems (sUAS). The paper provided an overview of chemical source localization approaches and how such approaches benefit from knowledge of atmospheric conditions, such as ambient winds and temperature. A Bayesian wind estimator was developed using an unscented Kalman filter. The process model used in the estimator was detailed and included terms appropriate for flight at potentially large advance and climb ratios. The wind estimator was demonstrated in a realistic simulation environment feature turbulent winds and dynamic plumes generated with the QUIC facility. Overall, the estimator was shown to accurately track the winds, even when the winds changed directions during the simulation. The wind estimator was combined with biologically-inspired source localization algorithms to locate the source in an urban environment. Future work will investigate formulating the estimator without rotor speed measurements, improving the estimation accuracy in the vertical axis, and evaluating the estimator in flight experiments. The approach can also be extended to swarms of sUAS, similar to the work in (Ref. 4).

ACKNOWLEDGEMENTS

This work was sponsored by a Small Business Technology Transfer project under contract FA8651-22-P-0089. The authors thank the program managers Dr. Jennifer Talley and Dr. Adam Rutkowski for their technical guidance and management.

REFERENCES

1. V. Pappu, Y. Liu, J. F. Horn, and J. Cooper, “Wind Gust Estimation on a Small VTOL UAV,” in 7th *AHS Technical Meeting on VTOL Unmanned Aircraft Systems and Autonomy*, AHS, January 2017.

2. Cooper, J., Schierman, J., and Horn, J. F., “Robust adaptive disturbance compensation for ship-based rotorcraft,” in *AIAA Guidance, Navigation, and Control Conference*, AIAA, 2010.

3. J. Gonzalez-Rocha, C. A. Woolsey, C. Sultan, S. de Wekker, and N. Rose, “Measuring Atmospheric Winds from Quadrotor Motion,” in *AIAA Atmospheric Flight Mechanics Conference*, p. 1189, 2017.

4. Cooper, Jared and Neal, David and De Wekker, Stephan, and Reed, Adam and Andrekanic, Alex and Paulini, Matthew, “Atmospheric Sampling in Urban Areas and Complex Terrain using UAS Swarms,” in 76th *Annual Forum of the Vertical Flight Society*, Vertical Flight Society, May 2020.

5. D. Etts, M. Rossi, R. Nzaou, R. Zhu, G. C. Lewin, and S. F. de Wekker, “Development of an Autonomous Multi-rotor Copter for Collecting Atmospheric Data near the Ground,” in *2015 Systems and Information Engineering Design Symposium*, pp. 120–124, IEEE, 2015.

6. T. Lewis and K. Bhaganagar, “A Comprehensive Review of Plume Source Localization Efforts Using Unmanned Vehicles for Environmental Sensing,” *Science of The Total Environment*, p. 144029, 2020.

7. G. Montes, B. Letheren, T. F. Villa, and F. Gonzalez, “Bio-inspired Plume Tracking Algorithm for UAVS,” in *Proceedings of the 16th Australasian Conference on Robotics and Automation 2014*, pp. 1–8, Australian Robotics and Automation Association Inc., 2014.

8. R. A. Russell, A. Bab-Hadiashar, R. L. Shepherd, and G. G. Wallace, “A Comparison of Reactive Robot Chemotaxis Algorithms,” *Robotics and Autonomous Systems*, vol. 45, no. 2, pp. 83–97, 2003.

9. P. P. Neumann, V. Hernandez Bennetts, A. J. Lilienthal, M. Bartholmai, and J. H. Schiller, “Gas Source Localization with a Micro-drone using Bio-inspired and Particle Filter-based Algorithms,” *Advanced Robotics*, vol. 27, no. 9, pp. 725–738, 2013.

10. H. M. Abdelghaffar, C. A. Woolsey, and H. A. Rakha, “Comparison of three approaches to atmospheric source localization,” *Journal of Aerospace Information Systems*, vol. 14, no. 1, pp. 40–52, 2017.

11. B. T. Michaelis, K. W. Leathers, Y. V. Bobkov, B. W. Ache, J. C. Principe, R. Baharloo, I. M. Park, and M. A. Reidenbach, “Odor tracking in aquatic organisms: the importance of temporal and spatial intermittency of the turbulent plume,” *Scientific Reports*, vol. 10, no. 1, pp. 1–11, 2020.

12. V. Jayaram, N. Kadakia, and T. Emonet, “Sensing complementary temporal features of odor signals enhances navigation of diverse turbulent plumes,” *Elife*, vol. 11, p. e72415, 2022.

13. S. R. Hanna, M. J. Brown, F. E. Camelli, S. T. Chan, W. J. Coirier, O. R. Hansen, A. H. Huber, S. Kim, and R. M. Reynolds, “Detailed simulations of atmospheric flow and dispersion in downtown manhattan: An application of five computational fluid dynamics models,” *Bulletin of the American Meteorological Society*, vol. 87, no. 12, pp. 1713–1726, 2006.

14. M. W. Rotach, “On the influence of the urban roughness sublayer on turbulence and dispersion,” *Atmospheric Environment*, vol. 33, no. 24-25, pp. 401–408, 1999.

15. H. Fernando, “Fluid dynamics of urban atmospheres in complex terrain,” *Annual review of fluid mechanics*, vol. 42, pp. 365–389, 2010.

16. G. M. Masters, *Introduction to Environmental Science and Engineering*. Upper Saddle River, NJ: Prentice-Hall, 2nd. Edition, 1997.

17. W. Johnson, *Helicopter Theory*. Courier Corporation, 2012.

18. R. W. Prouty, *Helicopter Performance, Stability, and Control*. 2002.

19. G. J. Leishman, *Principles of Helicopter Aerodynamics*. Cambridge university press, 2006.

20. J. V. Foster and D. Hartman, “High-fidelity Multi-rotor Unmanned Aircraft System (UAS) Simulation Development for Trajectory Prediction under off-nominal Flight Dynamics,” in *17th AIAA Aviation Technology, Integration, and Operations Conference*, p. 3271, 2017.

21. E. A. Morelli and V. Klein, *Aircraft system identification: theory and practice*, vol. 2. Sunflyte Enterprises Williamsburg, VA, 2016.

22. J. Cooper, T. Schlapkohl, E. A. Morelli, S. Roak, D. P. Gaublomme, B. Roberts, and S. Xiao, “Integrated Methods to Model and Update Rotorcraft Simulations with Experimental Data,” in *AHS* 70^{th} *Annual Forum*, (Montreal, Quebec), American Helicopter Society, May 2014.

23. C. M. Ivler, E. S. Rowe, J. Martin, M. J. Lopez, and M. B. Tischler, “System identification guidance for multirotor aircraft: Dynamic scaling and test techniques,” *Journal of the American Helicopter Society*, vol. 66, no. 2, pp. 1–16, 2021.

24. P. Niermeyer, T. Raffler, and F. Holzapfel, “Open-loop quadrotor flight dynamics identification in frequency domain via closed-loop flight testing,” in *AIAA Guidance, Navigation, and Control Conference*, p. 1539, 2015.

25. J. Cooper, V. S. Pappu, Y. Liu, and J. F. Horn, “Vehicle modeling for flight test measurements of ship airwake disturbances,” in *72nd American Helicopter Society International Annual Forum 2016: Leveraging Emerging Technologies for Future Capabilities*, pp. 2390–2408, American Helicopter Society, 2016.

26. M. A. Cunningham and J. E. Hubbard Jr, “Open-loop linear model identification of amultirotor vehicle with active feedback control,” *Journal of Aircraft*, vol. 57, no. 6, pp. 1044–1061, 2020.

27. S. Sun, C. C. de Visser, and Q. Chu, “Quadrotor graybox model identification from high-speed flight data,” *Journal of Aircraft*, vol. 56, no. 2, pp. 645–661, 2019.

28. E. A. Morelli, “Efficient Global Aerodynamic Modeling from Flight Data,” in 50^{th} *AIAA Aerospace Sciences Meeting including the New Horizons Forum and Aerospace Exposition*, (Nashville, Tennessee), AIAA 2012-1050, January 2012.

29. R. V. Jategaonkar, *Flight Vehicle System Identification: A Time Domain Methodology*. American Institute of Aeronautics and Astronautics, 2006.

30. S. J. Julier and J. K. Uhlmann, “New Extension of the Kalman Filter to Nonlinear Systems,” in *Signal Processing, Sensor Fusion, and Target Recognition VI*, vol. 3068, pp. 182–193, Spie, 1997.

31. S. J. Julier and J. K. Uhlmann, “Unscented Filtering and Nonlinear Estimation,” *Proceedings of the IEEE*, vol. 92, no. 3, pp. 401–422, 2004.

32. E. A. Wan and R. Van Der Merwe, “The Unscented Kalman Filter for Nonlinear Estimation,” in *Proceedings of the IEEE 2000 Adaptive Systems for Signal Processing, Communications, and Control Symposium (Cat. No. 00EX373)*, pp. 153–158, Ieee, 2000.

33. A. Bateman, S. De Wekker, and e. a. DeVore, Michael, “Turbulence Modeling and Risk-based Planning,” NASA SBIR Phase II Final Technical Report, Barron Associates,Inc., May 2022.

34. M. J. Brown, “Urban Dispersion: Challenges for Fast Response Modeling,” Technical Report, Los Alamos National Laboratory, 2004.

35. M. D. Williams, M. J. Brown, and A. Gowardhan, “Adaptation of the QUIC-PLUME Model for Heavy Gas Dispersion Around Buildings,” in *Atmospheric Sciences and Air Quality Conferences (ASAAQ2005-8.6)*, 2005.

36. M. J. Brown, “Quick Urban and Industrial Complex (QUIC) CBR Plume Modeling System: Validation-Study Document,” October 2018.

APPENDIX

PARAMETER ESTIMATES FOR IDENTIFIED MODEL

This appendix lists the parameter values for the identified vehicle model.

Parameter	Estimate		95% CI
$C_{X_{H_\mu}}$	-1.6667e-02	$\pm$	1.5112e-04
$C_{X_{H_{\mu^2}}}$	-6.1079e-04	$\pm$	3.3836e-04
$C_{X_{H_{\mu\mu_z}}}$	7.3582e-02	$\pm$	2.7079e-03
$C_{Y_{H_\mu}}$	-1.6714e-02	$\pm$	2.0943e-04
$C_{Y_{H_{\mu^2}}}$	-5.9325e-04	$\pm$	4.3847e-04
$C_{Y_{H_{\mu\mu_z}}}$	1.2305e-01	$\pm$	3.7745e-03
$C_{Z_{T_0}}$	1.1429e-02	$\pm$	3.5852e-05
$C_{Z_{T_\nu}}$	1.7573e-03	$\pm$	2.2883e-04
$C_{Z_{T_\mu}}$	-1.1186e-03	$\pm$	5.5328e-04
$C_{Z_{T_{\mu_z}}}$	2.0740e-02	$\pm$	6.4645e-04
$C_{Z_{T_{\mu^2}}}$	-4.9559e-02	$\pm$	8.1743e-03
$C_{l_{T_0}}$	1.3499e-02	$\pm$	5.0575e-04
$C_{l_{T_\nu}}$	1.1926e-02	$\pm$	6.4505e-03
$C_{l_{T_\mu}}$	-8.2076e-02	$\pm$	2.4614e-03
$C_{l_{H_\mu}}$	-6.0748e-02	$\pm$	2.4487e-03
$C_{l_{H_{\mu\mu_z}}}$	8.6538e-01	$\pm$	4.2517e-02
$C_{l_{H_{\mu\nu}}}$	6.0638e-02	$\pm$	1.5743e-02
$C_{l_{p,\delta t}}$	-2.0113e-02	$\pm$	1.7887e-03
$C_{m_{T_0}}$	1.2171e-02	$\pm$	4.6460e-04
$C_{m_{T_\nu}}$	1.5551e-02	$\pm$	6.0196e-03
$C_{m_{T_\mu}}$	-1.3047e-01	$\pm$	2.2997e-03
$C_{m_{H_\mu}}$	-5.7710e-02	$\pm$	2.4691e-03
$C_{m_{H_{\mu\mu_z}}}$	2.7172e-01	$\pm$	5.0298e-02
$C_{m_{H_{\mu\nu}}}$	2.4182e-02	$\pm$	1.6178e-02
$C_{m_{q,\delta t}}$	-2.9036e-02	$\pm$	1.8506e-03
$C_{n_{Q_0}}$	1.3812e-02	$\pm$	6.7550e-04
$C_{n_{Q_\nu}}$	-3.3331e-02	$\pm$	8.4754e-03
$C_{n_{H_\mu}}$	-7.2825e-02	$\pm$	2.7042e-03
$C_{n_{r,\delta t}}$	-1.1517e+00	$\pm$	2.0571e-02

Table 5. Parameter estimates